

Untangling the solar wind and magnetospheric drivers of the radiation belt electrons

Simon Wing¹, Jay Robert Johnson², Drew L. Turner³, Aleksandr Ukhorskiy⁴, and Alexander J. Boyd⁵

¹Johns Hopkins University

²Andrews University

³The Johns Hopkins University Applied Physics Laboratory

⁴JHU/APL

⁵The Aerospace Corporation

November 22, 2022

Abstract

Many solar wind parameters correlate with one another, which complicates the causal-effect studies of solar wind driving of the magnetosphere. Conditional mutual information (CMI) is used to untangle and isolate the effect of individual solar wind and magnetospheric drivers of the radiation belt electrons. The solar wind density (n_{sw}) negatively correlates with electron phase space density (PSD) (average energy ~ 1.6 MeV) with time lag (t) = 15 hr. This effect of n_{sw} on PSD has been attributed to magnetopause shadowing losses, but when the effect of solar wind velocity (V_{sw}) is removed, t shifts to 7–11 hr, which is a more accurate time scale for this process. The peak correlation between V_{sw} and PSD shifts from $t = 38$ to 46 hr, when the effect of n_{sw} is removed. This suggests that the time scale for electron acceleration to 1–2 MeV is about 46 hr following V_{sw} enhancements. The effect of n_{sw} is significant only at $L^* = 4.5$ –6 ($L^* > 6$ is highly variable) whereas the effect of V_{sw} is significant only at $L^* = 3.5$ –6.5. The peak response of PSD to V_{sw} is the shortest and most significant at $L^* = 4.5$ –5.5. As time progresses, the peak response broadens and shifts to higher t at higher and lower L^* , consistent with local acceleration at $L^* = 4.5$ –5.5 followed by outward and inward diffusion. The outward radial diffusion time scale at $L^* = 5$ –6 is ~ 40 hr per R_E .

1 Untangling the solar wind and magnetospheric drivers of the radiation belt electrons

2 Simon Wing¹, Jay R. Johnson², Drew L. Turner¹, Aleksandr Y. Ukhorskiy¹, and
3 Alexander J. Boyd³
4

5 ¹The Johns Hopkins University, Applied Physics Laboratory, Laurel, Maryland, USA

6 ²Andrews University, Berrien Spring, Michigan, USA

7 ³The Aerospace Corporation, El Segundo, California, USA
8

9 **Abstract.** Many solar wind parameters correlate with one another, which complicates the causal-
10 effect studies of solar wind driving of the magnetosphere. Conditional mutual information (CMI)
11 is used to untangle and isolate the effect of individual solar wind and magnetospheric drivers of
12 the radiation belt electrons. The solar wind density (n_{sw}) negatively correlates with electron phase
13 space density (PSD) (average energy ~ 1.6 MeV) with time lag (τ) = 15 hr. This effect of n_{sw} on
14 PSD has been attributed to magnetopause shadowing losses, but when the effect of solar wind
15 velocity (V_{sw}) is removed, τ shifts to 7–11 hr, which is a more accurate time scale for this process.
16 The peak correlation between V_{sw} and PSD shifts from $\tau = 38$ to 46 hr, when the effect of n_{sw} is
17 removed. This suggests that the time scale for electron acceleration to 1–2 MeV is about 46 hr
18 following V_{sw} enhancements. The effect of n_{sw} is significant only at $L^* = 4.5$ –6 ($L^* > 6$ is highly
19 variable) whereas the effect of V_{sw} is significant only at $L^* = 3.5$ –6.5. The peak response of PSD
20 to V_{sw} is the shortest and most significant at $L^* = 4.5$ –5.5. As time progresses, the peak response
21 broadens and shifts to higher τ at higher and lower L^* , consistent with local acceleration at $L^* =$
22 4.5–5.5 followed by outward and inward diffusion. The outward radial diffusion time scale at L^*
23 = 5–6 is ~ 40 hr per R_E .

24
25 ORCID ID: 0000-0001-9342-1813

26 **Plain Language Summary**

27 Many solar wind parameters correlate with one another, which complicates the causal-effect
28 studies of solar wind driving of the magnetosphere. We use conditional mutual information (CMI),
29 which is part of information theory, to untangle and isolate the effect of individual solar wind and
30 magnetospheric drivers of the radiation belt electrons. For example, the solar wind density
31 negatively correlates with electron phase space density (PSD) (average energy ~ 1.6 MeV) with
32 the response time lag of 15 hours. This has been attributed to the electron loss process called
33 magnetopause shadowing. The time lag suggests the time scale for this process is 15 hours.
34 However, when the effect of solar wind velocity is removed, the time lag is 7–11 hours, which is
35 a more accurate time scale for this process. As another example, the time lag of the correlation
36 between solar wind velocity and PSD shifts 38 to 46 hours, when the effect of solar wind density
37 is removed. This suggests that the time scale for electron acceleration to 1–2 MeV is about 46
38 hours following the solar wind velocity enhancements. We also show that the effects of solar wind
39 velocity and density have dependence on radial distance.

40

41 **Keywords:** radiation belt, relativistic electrons, solar wind drivers, nonlinear relationships,
42 information theory, local acceleration, diffusion time scale, electron acceleration, magnetopause
43 shadowing.

44 **Index terms:** 2774, 2784, 2720, 2730, 4499

45 **Major science question:**

46 **New Science knowledge:**

47 **Broad Implications:** Information theoretical tools can be useful to untangle and isolate individual
48 solar wind and magnetospheric drivers of the radiation belt.

49 **Key points:** (1) The effect of n_{sw} on radiation belt electrons is significant only at $L^* = 4.5-6$ and
50 not significant at $L^* < 3$. (2) The effect of V_{sw} on radiation belt electrons is significant at $L^* =$
51 $3.5-6.5$ and not significant at $L^* < 3.5$. (3) The radiation belt response time lag to V_{sw} suggests
52 local acceleration at $L^* = 4.5-5.5$ followed by outward and inward diffusion.

53

54 1. Introduction

55 The Earth's radiation belt is populated by electrons having energies of hundreds of keVs
56 to >10 MeVs. These electrons are hazardous to satellites that encounter them in the inner-
57 magnetosphere $r \sim 2-8 R_E$, including at the geosynchronous orbit (GEO), and at their foot points at
58 low earth orbit (LEO) in the ionosphere, where $1 R_E =$ radius of the Earth = 6372 km. The MeV
59 electrons can penetrate deep into spacecraft leading to spacecraft or instrument malfunctions while
60 those with energies < 1 MeV can accumulate on the surface of the spacecraft bodies, leading to
61 electrical discharges.

62 It has long been recognized that the variabilities of the radiation belt electrons, to a large
63 extent, are driven by the solar wind (e.g., *Baker et al.*, 1990, 2018; 2019a; *Li et al.*, 2001; 2005;
64 *Reeves*, 2007; *Ukhorskiy et al.*, 2004; *Turner and Li*, 2008, *Reeves et al.*, 2013; *Xiang et al.*, 2017;
65 *Pinto et al.*, 2018; *Zhao et al.*, 2017, *Alves et al.*, 2017). However, many solar wind parameters
66 positively and negatively correlate with one another, which can complicate the interpretation of
67 the solar wind drivers of the radiation belt (e.g., *Hundhausen et al.*, 1970; *Wing et al.*, 2016; *Wing*
68 *and Johnson*, 2019; *Borovsky*, 2012; 2016; 2018; 2020; *Maggiolo et al.*, 2017). For example, solar
69 wind velocity (V_{sw}) positively correlates with radiation belt electron fluxes (J_e) (e.g., *Baker et al.*,
70 1990; *Reeves et al.*, 2011; *Balikhin et al.*, 2011; *Paulikas and Blake*, 1979; *Li et al.*, 2001; 2005;
71 *Wing et al.*, 2016). Solar wind density (n_{sw}) negatively correlates with radiation belt J_e (e.g., *Li et*
72 *al.*, 2005; *Lyatsky and Kazanov*, 2008a; *Kellerman and Shprits*, 2012; *Rigler et al.*, 2007; *Balikhin*
73 *et al.*, 2011; *Wing et al.*, 2016). However, V_{sw} negatively correlates with n_{sw} (e.g., *Wing et al.*,
74 2016; *Borovsky*, 2020). This raises the question that given the V_{sw} - n_{sw} negative correlation, if V_{sw}
75 positively correlates with radiation belt electron J_e , then the negative correlation of n_{sw} with
76 radiation belt electron J_e may simply be coincidental. Conversely, given the solar wind property,

77 if n_{sw} negatively correlates with J_e , then the positive correlation of V_{sw} and radiation belt J_e may
78 simply be coincidental. Of course, n_{sw} and V_{sw} may independently exert influence on the radiation
79 belt electrons. In that case, how can one isolate the effect of an individual solar wind parameter?

80 A few studies attempted to separate the effects of n_{sw} from V_{sw} by using methods that bin
81 the data into small intervals of V_{sw} and n_{sw} or explicitly select events when one parameter is nearly
82 constant while the effect of the other parameter is investigated (e.g., *Lyatsky and Khazanov,*
83 2008a). This type of analysis has offered insights into the solar wind driving of the radiation belt
84 J_e . However, holding one parameter nearly constant, either explicitly or through small binning, in
85 order to investigate the second parameter does not completely eliminate the effect of the first
86 parameter. For example, selecting events when V_{sw} is nearly constant to investigate the effect of
87 n_{sw} does not completely eliminate the effect of V_{sw} because V_{sw} or its effect is not zero. Nearly
88 constant but high V_{sw} can still affect the correlation of n_{sw} and radiation belt J_e . Moreover, it does
89 not address the question of how much additional information n_{sw} provides to J_e , given V_{sw} and vice
90 versa. Many studies have shown that other solar wind parameters and magnetospheric parameters
91 can also contribute to J_e variations [e.g., *Balikhin et al., 2011; Rigler et al., 2007; Vassiliadis et*
92 *al., 2005; Li et al., 2005; Onsager et al., 2007; Simms et al., 2014;*], but presently, it is not entirely
93 clear quantitatively given a main driver, e.g., V_{sw} (or n_{sw}), how much additional information these
94 parameters provide to J_e .

95 The solar wind–radiation belt systems have been shown to be nonlinear [e.g., *Wing et al.,*
96 2005; *Johnson and Wing, 2005; Reeves et al., 2011; Kellerman and Shprits, 2012; Wing et al.,*
97 2016]. For nonlinear system, linear correlational analysis can be misleading [e.g., *Balikhin et al.,*
98 2010; 2011].

99 Information theory has been shown to be quite useful for studies of the Earth’s

100 magnetosphere (*Balasis et al.*, 2008; 2009; 2011; 2013; *Stumpo et al.*, 2020; *Materassi et al.*, 2011,
101 *De Michelis et al.*, 2011, 2017; *March et al.*, 2005; *Johnson and Wing*, 2005; 2014, *Wing et al.*,
102 2016; *Johnson et al.*, 2018; *Wing and Johnson*, 2019; *Runge et al.*, 2018; *Papadimitriou et al.*,
103 2020; *Manshour et al.*, 2021), Kronian magnetosphere (*Wing et al.*, 2020), and the Sun (*Consolini*
104 *et al.*, 2009; *Wing et al.*, 2018; *Snelling et al.*, 2020). Information theory can help identify
105 nonlinearities in the system and information transfer from one variable to another. Moreover,
106 information theory can also help untangle the drivers that are positively or negatively correlated
107 with one another (*Wing et al.*, 2016; *Wing and Johnson*, 2019).

108 *Wing et al.* (2016) used information theoretic tools to study the solar wind driving of the
109 radiation belt electrons. The study used the publicly available Los Alamos National Laboratory
110 (LANL) satellite data, which provide geosynchronous electron flux measurements at daily
111 resolution. When the study began in early 2015, the Radiation Belt Storm Probes (RBSP) or Van
112 Allen Probes satellites had only been operational for a few years, and there was not enough data
113 for a statistical study. Usage of the daily resolution of the radiation belt electron data prevented
114 *Wing et al.* (2016) from resolving any electron response lag time to the solar wind drivers that is
115 shorter than 24 hours. For example, the LANL MeV electron J_e negatively correlates with daily
116 averaged n_{sw} with a lag time (τ) of 1 day. *Zhao et al.* (2017) correlated daily averaged radiation
117 belt electron phase space density (PSD) with n_{sw} and also obtained $\tau = 1$ day for MeV electrons (μ
118 > 700 MeV G⁻¹). However, if the effect of V_{sw} is properly removed, τ shifts to 0 day (*Wing et al.*,
119 2016). In other words, the radiation belt electron response to n_{sw} is less than 24 hr. However, the
120 study could not pinpoint exactly how much less than 24 hr with the daily resolution LANL data.
121 Another limitation of *Wing et al.* (2016) study is that the LANL data only provide the electron
122 observations at a fixed radial distance from the Earth, at the geosynchronous orbit.

123 Since *Wing et al.* (2016) study, RBSP has gathered seven years of radiation belt electron
124 data (2013-2019) at high time resolution (< 1 min) from $2 < L^* < 7$. Hence, the time is ripe for a
125 follow up study that uses the RBSP data. As in *Wing et al.* (2016), the present study uses
126 information theory to determine the solar wind and magnetospheric drivers of the radiation belt
127 electrons and the response time scales. In order to focus on the drivers of the nonadiabatic heating
128 and acceleration, the present study examines the response of the radiation belt electron phase space
129 density (PSD) to the drivers.

130

131 **2. Data set**

132 Van Allen Probe (or RBSP) mission, which was launched in 2012, had two identically
133 instrumented spacecraft in near-equatorial orbit (about 10° inclination) with perigee at 600 km
134 altitude and apogee at $5.8 R_E$ geocentric (*Mauk et al.*, 2013). The MAGnetic Electron Ion
135 Spectrometer (MagEIS) and Relativistic Electron-Proton Telescope (REPT) instruments are part
136 of the Energetic particle, Composition, and Thermal plasma Suite (ECT) instrument on board of
137 RBSP (*Spence et al.*, 2013). MagEIS measured the energy range of 30 keV to 4 MeV for electrons
138 and 20 keV to 1 MeV for ions (*Blake et al.*, 2013) while REPT measured electrons with energy
139 range 1.5 to ≥ 10 MeV and protons with energy range 20 to 75 MeV (*Baker et al.*, 2012).

140 The present study focuses only on the electron data. Radiation belt electron dynamics can
141 often be described by their adiabatic invariants and PSD (μ , K , L^*) where μ = the first adiabatic
142 invariant related to the gyromotion perpendicular to the magnetic field line, K = the second
143 adiabatic invariant related to the bounce motion along the field line, and L or L^* = the third
144 adiabatic invariant related to the curvature and gradient drift motion around the Earth (actually L^*
145 is inversely proportional to the third invariant Φ) (*Roederer*, 1970; *Schulz and Lanzerotti*, 1974;

146 *Lejosne and Kollman, 2020*).

147 Data from the RBSP-ECT Combined dataset (Boyd et al., 2021) are used to obtain electron
148 PSD as a function of adiabatic invariants across the full MagEIS and REPT energy range. The
149 PSD is calculated using the techniques outlined in (*Turner et al., 2014a; 2014b; Boyd et al., 2014*)
150 at ~ 5 min time cadence. We select the electrons with $\mu = 725\text{--}875$ MeV G $^{-1}$ and $K = 0.09\text{--}0.13$
151 R_E G $^{-0.5}$. These electrons have an average energy of ~ 1.6 MeV, but they range from 480 keV to
152 4.8 MeV spanning over L^* of 2.5 to 6.8.

153 The solar wind, AL, and SYM-H data 2013-2019 come from OMNI 1 min resolution data
154 provided by NASA (<http://omniweb.gsfc.nasa.gov/>). Both the PSD and OMNI data 2013-2019
155 are averaged with 30 min sliding window.

156 We merge each OMNI solar wind parameter (V_{sw} , n_{sw} etc.) with the RBSP electron PSD.
157 As described in Section 3, we perform time shifted correlation and conditional mutual information
158 analysis to determine the radiation belt electron response lag time up to 120 hr. Depending on the
159 solar wind parameter, typically the merged datasets have approximately 60,000 to 85,000 points.

160

161 **3. Methodology**

162 Mutual information and conditional mutual information are briefly described below, but
163 they are also described in *Balasis et al. (2013)*, and *Wing et al. (2016, 2018)*.

164 Mutual information (MI) (*Tsonis, 2001; Li, 1990; Darbellay and Vajda, 1999*) between
165 two variables, x and y , compares the uncertainty of measuring variables jointly with the uncertainty
166 of measuring the two variables independently. The uncertainty is measured by Shannon entropy.
167 In order to construct the entropies, it is necessary to obtain the probability distribution functions,
168 which in this study are obtained from histograms of the data based on discretization of the variables

169 (i.e. bins).

170 Suppose that two variables, x and y , are binned so that they take on discrete values, \hat{x} and
171 \hat{y} , where

$$172 \quad x \in \{\hat{x}_1, \hat{x}_2, \dots, \hat{x}_n\} \equiv \aleph_1; \quad y \in \{\hat{y}_1, \hat{y}_2, \dots, \hat{y}_m\} \equiv \aleph_2 \quad (1)$$

173 The variables may be thought of as letters in alphabets \aleph_1 and \aleph_2 , which have n and m letters,
174 respectively. The extracted data can be considered as sequences of letters. The entropy associated
175 with each of the variables is defined as

$$176 \quad H(x) = - \sum_{\aleph_1} p(\hat{x}) \log p(\hat{x}); \quad H(y) = - \sum_{\aleph_2} p(\hat{y}) \log p(\hat{y}) \quad (2)$$

177 where $p(\hat{x})$ is the probability of finding the word \hat{x} in the set of x -data and $p(\hat{y})$ is the probability
178 of finding word \hat{y} in the set of y -data. To examine the relationship between the variables, we
179 extract the word combinations (\hat{x}, \hat{y}) from the dataset. The joint entropy is defined by

$$180 \quad H(x, y) = - \sum_{\aleph_1 \aleph_2} p(\hat{x}, \hat{y}) \log p(\hat{x}, \hat{y}) \quad (3)$$

181 where $p(\hat{x}, \hat{y})$ is the probability of finding the word combination (\hat{x}, \hat{y}) in the set of (x, y) data.

182 The mutual information is then defined as

$$183 \quad MI(x, y) = H(x) + H(y) - H(x, y) \quad (4)$$

184 While MI is useful to identify nonlinear dependence between two variables, it is often
185 useful to consider conditional dependency with respect to a conditioner variable z that takes on
186 discrete values, $\hat{z} \in \{z_1, z_2, \dots, z_n\} \equiv \aleph_3$. The conditional mutual information (Wyner, 1978)

$$187 \quad CMI(x, y | z) = \sum_{\aleph_1 \aleph_2 \aleph_3} p(\hat{x}, \hat{y}, \hat{z}) \log \frac{p(\hat{x}, \hat{y} | \hat{z})}{p(\hat{x} | \hat{z}) p(\hat{y} | \hat{z})} = H(x, z) + H(y, z) - H(x, y, z) - H(z) \quad (5)$$

188 determines the mutual information between x and y given that z is known. In the case where z is
189 unrelated, $CMI(x, y | z) = MI(x, y)$, but in the case that x or y is known based on z , then $CMI(x, y | z)$
190 $= 0$. CMI therefore provides a way to determine how much additional information is known given
191 another variable. CMI can be seen as a special case of the more general conditional redundancy

192 that allows the variable z to be a vector (e.g., *Prichard and Theiler, 1995; Johnson and Wing,*
193 2014).

194 Herein, we use the short hand Pearson's linear correlation $\text{corr}(x(t), y(t + \tau))$ as $\text{corr}(x \rightarrow$
195 $y)$. Likewise, $\text{CMI}(x(t), y(t + \tau) | z(t))$ is denoted as $\text{CMI}(x \rightarrow y | z)$. We define i_{tr} = information
196 transfer = $\text{CMI}(x \rightarrow y | z) - \text{mean noise}$, where $\text{noise} = \text{CMI}(\text{sur}(x) \rightarrow y | z)$, $\text{sur}(x)$ is the surrogate
197 data of x and is obtained by randomly permuting the order of the time series of array x . Mean and
198 σ of the noise are calculated from an ensemble of 100 values of $\text{CMI}(\text{sur}(x) \rightarrow y | z)$. The mean
199 noise and σ estimate are valuable diagnostics included on all of the CMI data presented here: any
200 CMI outside the 3σ noise range are significant and CMI less than the 3σ from the noise is
201 considered not significant. Furthermore, we define $i_{tr_max} = i_{tr}$ at the peak τ and significance =
202 i_{tr}/σ .

203

204 **4. Applying information theory to radiation belt MeV electron data**

205 **4.1 A simple example of an application of conditional mutual information (CMI)**

206 CMI can be quite useful to untangle the effects of multiple drivers of a system. Figure 1
207 presents a simple example that illustrates this point. Figure 1a plots $\text{corr}(V_{sw} \rightarrow \text{PSD})$. The figure
208 shows that V_{sw} positively correlates with PSD and the correlation peaks at $\tau = 38$ hr. The
209 correlation is significant with $n = 84,729$ points and correlation coefficient (r) = 0.47 and $p < 0.01$.
210 Previous studies have also found good correlations between V_{sw} and radiation belt electrons with
211 ~ 2 days lag and the lag time has been attributed to the time scale to accelerate the electrons to 1–
212 2 MeV due to local acceleration, radial transport, or some other acceleration mechanisms (e.g.,
213 *Baker et al., 1990; Shprits et al., 2008; 2009; Reeves et al., 2011; 2013; Li et al., 2005; Ukhorskiy*
214 *et al., 2005; Wing et al., 2016; Summers et al., 2007; Thorne et al., 2013; Newell et al., 2016;*

215 *Turner and Li, 2008; Boyd et al., 2016; 2018*). Figure 1b plots the $\text{corr}(n_{sw} \rightarrow \text{PSD})$, which shows
216 that n_{sw} negatively correlates with PSD with a minimum at $\tau = 15$ hr, $r = -0.22$, $n = 84,729$, $p <$
217 0.01 . *Lyatsky and Khazanov (2008a)* also found the same negative correlation at $\tau = 15$ hr. The
218 negative correlation has been previously attributed to the magnetopause shadowing effect: an
219 increase in n_{sw} would increase solar wind dynamic pressure (P_{dyn}), which would compress the
220 magnetosphere leading to radiation belt electron losses (e.g., *Li et al., 2001; Kellerman and*
221 *Shprits, 2012; Turner et al., 2012; Ukhorskiy et al., 2006*). Figure 1c plots the $\text{corr}(P_{dyn} \rightarrow \text{PSD})$,
222 which shows that the radiation belt electron response to P_{dyn} , which is $\sim n_{sw} V_{sw}^2$, has dual modes.
223 At small τ , $\tau < \sim 20$ hr, P_{dyn} negatively correlates with PSD, which is similar to the effect of n_{sw}
224 and can be attributed to the magnetopause shadowing effect. However, at large τ , $\tau > 40$ hr, P_{dyn}
225 positively correlates with PSD, which is similar to the effect of V_{sw} . The correlations are significant
226 at $p < 0.01$ and $n = 82,652$. *Zhao et al. (2017)* correlated P_{dyn} with PSD at daily time resolution
227 and also found a dual response mode of the PSD to P_{dyn} . Figure 1d plots $\text{CMI}(P_{dyn} \rightarrow \text{PSD} | n_{sw})$,
228 which shows the dependence of PSD on P_{dyn} , given n_{sw} . It shows that if we remove the effect of
229 n_{sw} , the effect of P_{dyn} on PSD is similar to that of V_{sw} in Figure 1a, as expected. The CMI curve
230 does not match exactly the correlation curve in Figure 1a because the CMI curve takes into account
231 the nonlinearities in the data.

232 In Figure 1d, the green solid and dashed curves are mean noise and 3σ from the noise,
233 respectively. The significance at peak $\tau = 51$ hr is 203σ and hence it is significant.

234

235 **4.2 Isolating the effects of the solar wind velocity from density and vice versa**

236 *Wing et al. (2016)* isolated the effects of V_{sw} and n_{sw} on the radiation belt electron J_e using
237 CMI. They found that $\text{CMI}(V_{sw} \rightarrow J_e | n_{sw})$ peaks at $\tau = 2$ -3 days while $\text{CMI}(n_{sw} \rightarrow J_e | V_{sw})$ peaks

238 at $\tau = 0$ day. However, the lag times, τ , in *Wing et al. (2016)* are imprecise due to the usage of the
 239 daily resolution LANL electron data. Furthermore, LANL data are limited to GEO, but the outer
 240 belt is not accurately represented by data at GEO alone, especially for the heart of the outer belt
 241 between $4 \leq L \leq 5$ (e.g., *Baker et al., 2019b*). In the present study, we recompute the CMIs using
 242 30 min resolution RBSP PSDs representative of ~ 1 MeV electrons throughout the entire outer belt
 243 and solar wind data. Furthermore, by using electron PSD for fixed values of the first and second
 244 adiabatic invariants in place of J_e as a function of energy, the data used here further deconvolute
 245 the energy and pitch angle dependencies of the underlying physical processes that drive radiation
 246 belt enhancements and losses.

247 Figures 2a and 2b replot $\text{corr}(V_{sw} \rightarrow \text{PSD})$ and $\text{corr}(n_{sw} \rightarrow \text{PSD})$, which are plotted in
 248 Figures 1a and 1b, respectively. However, V_{sw} negatively correlates with n_{sw} and $\text{corr}(V_{sw} \rightarrow n_{sw})$
 249 has a minimum at $\tau = 15$ hr ($r = -0.48$, $n = 105,459$, $p < 0.01$), as shown in Figure 2c. For
 250 completeness, Figure 2c also plots $\text{corr}(n_{sw} \rightarrow V_{sw})$ (red curve), which has $r = 0.10$, $p < 0.01$. The
 251 figure shows that $|\text{corr}(V_{sw} \rightarrow n_{sw})| > |\text{corr}(n_{sw} \rightarrow V_{sw})|$. The negative correlation between V_{sw} and
 252 n_{sw} have been previously reported with similar τ (e.g., *Wing et al., 2016; Maggiolo et al., 2017;*
 253 *Borovsky, 2020*). Note that τ may vary from year to year (*Wing et al., 2016*), leading to an overall
 254 broadening of the peak when considering an ensemble of intervals across the solar cycle.

255 Given that V_{sw} negatively correlates with n_{sw} , if n_{sw} negatively correlates with PSD (Figure
 256 2b), then the positive correlation between V_{sw} and PSD may be deemed just coincidental. To check
 257 on this possibility, we compute $\text{CMI}(V_{sw} \rightarrow \text{PSD} | n_{sw})$, which is plotted in Figure 2d. The figure
 258 shows that even after the effect of n_{sw} has been removed, there is still strong information transfer
 259 from V_{sw} to PSD, which peaks at $\tau = 46$ hr ($n = 78,811$, significance = 378σ). Apparently,
 260 removing the effect of n_{sw} , shifts the peak to the right. The lag time of $\tau = 46$ hr obtained from

261 CMI is considered a more accurate radiation belt electron response time to the V_{sw} (the time scale
262 for electron acceleration to 1-2 MeV energy range) than the lag time of $\tau = 38$ hr obtained from
263 Pearson's correlation.

264 We can also check whether or not $\text{corr}(n_{sw} \rightarrow \text{PSD})$ is coincidental, given the V_{sw} negative
265 correlation with n_{sw} and V_{sw} positive correlation with PSD. Figure 2e plots $\text{CMI}(n_{sw} \rightarrow \text{PSD} | V_{sw})$,
266 which shows two peaks. The primary peak at $\tau = 7-11$ hr ($n = 78,811$, significance = 52σ) can be
267 compared to the minimum in $\text{corr}(n_{sw} \rightarrow \text{PSD})$ in Figure 2b. Apparently, removing the effect of
268 V_{sw} , shifts the peak to the left. The lag time of $\tau = 7-11$ hr is considered a more accurate radiation
269 belt electron response time to the magnetopause shadowing effect than the $\tau = 15$ hr obtained from
270 the correlational analysis. Note that CMI only gives positive values and does not distinguish
271 negative from positive correlations. As such, CMI is analogous to $|r|$.

272 Figure 2e shows that there is a secondary broad peak at $\tau = 80-120$ hr (or even larger).
273 Unlike the primary peak, which is a negative correlation, the secondary peak is a positive
274 correlation with n_{sw} . In order to show this, we plot $\text{PSD}(t + \tau)$ vs. $V_{sw}(t)$ vs. $n_{sw}(t)$ for $\tau = 0, 5, 10,$
275 $40, 80, 100,$ and 120 hr in Figure 3 panels a to g, respectively. In all panels, it can be seen that at
276 high V_{sw} , $V_{sw} > \sim 500$ km s⁻¹, V_{sw} positively correlates with the radiation belt electron PSD as
277 previously reported (Reeves *et al.*, 2011; Li *et al.*, 2001; Kellerman and Shprits, 2012; Wing *et al.*,
278 2016). However, for $V_{sw} < \sim 450$ km s⁻¹, and small τ ($\tau = 0, 5,$ and 10 hr), n_{sw} negatively correlates
279 with the radiation belt electron PSD, which is consistent with the first and primary peak of $\text{CMI}(n_{sw}$
280 $\rightarrow \text{PSD} | V_{sw})$ in Figure 2e, which can be attributed to the magnetopause shadowing effect. At $\tau =$
281 40 hr, there is little or no correlation between n_{sw} and the PSD, which is consistent with the
282 minimum of $\text{CMI}(n_{sw} \rightarrow \text{PSD} | V_{sw})$ in Figure 2e. However, at large τ , $\tau = 80, 100, 120$ hr and V_{sw}
283 $< \sim 450$ km s⁻¹, n_{sw} positively correlates with PSD, which is consistent with the secondary peak in

284 Figure 2e. This positive correlation between n_{sw} and electron PSD at large τ cannot be seen in the
285 $\text{corr}(n_{sw} \rightarrow \text{PSD})$ in Figure 2b because the effect has been smeared or cancelled out by the effects
286 for all V_{sw} where high electron PSD can correspond to high and low n_{sw} (Figure 3 panels e–g).

287 It is not clear what causes the positive linear and nonlinear correlation between n_{sw} and
288 electron PSD at large τ . n_{sw} may be a proxy for another parameter. As an example, n_{sw} positively
289 correlates with |IMF B| (peak $\tau = 6$ hr, $r \sim 0.40$, $n = 105,923$, $p < 0.01$) as plotted in Figure 4a,
290 which has implications for the radiation belt electrons. This correlation has been previously
291 observed (*Borovsky, 2020; Maggiolo et al., 2017*). Larger n_{sw} would correspond to more negative
292 IMF B_z when IMF B_z is southward (IMF $B_z < 0$) and more positive IMF B_z when IMF B_z is
293 northward (IMF $B_z > 0$), as shown in Figures 4b and 4c, respectively. Figure 4b shows that n_{sw}
294 negatively correlates with southward IMF (peak $\tau = 6$ hr, $r = 0.3$, $n = 54,265$, $p < 0.01$) while
295 Figure 4c shows that n_{sw} positively correlates with northward IMF (peak $\tau = 8$ hr, $r = 0.3$, $n =$
296 $51,388$, $p < 0.01$). The n_{sw} negative correlation with IMF $B_z < 0$ would be relevant to the discussion
297 of the effect n_{sw} on the radiation belt electrons because prolonged southward IMF can lead to
298 substorms (e.g., *Birn and Hones, 1981; Rostoker, 1983; McPherron et al., 1986; McPherron, 1991;*
299 *Lui, 1991; Lyons, 1995; Lyons et al., 1997; Johnson and Wing, 2014; Birn et al., 1997; 2006*),
300 which in turn can lead to injections of seed electrons, enhanced chorus wave activity, and the
301 growth of the MeV radiation belt electrons (e.g., *Miyoshi et al., 2013; Jaynes et al., 2015; see*
302 *Section 5.3*).

303 n_{sw} may also be correlated or be a proxy for other solar wind parameters. For example,
304 *Kepko et al. (2019)* reported that a sharp density increase can be accompanied by quasiperiodic
305 density fluctuations that can lead to the growth of the globally coherent magnetospheric ultralow
306 frequency (ULF) waves, which can, in turn, accelerate radiation belt electrons (e.g., *Matthie and*

307 *Mann, 2000; O'Brien et al., 2003; Ukhorskiy et al., 2005; Hudson et al., 2008; Li et al., 2009;*
 308 *Mann et al., 2016; Zhao et al., 2018; Jaynes et al., 2018).* Hence, the long range correlation of
 309 (n_{sw} , PSD) and (IMF $B_z > 0$, PSD) may be attributed to the density fluctuations and ULF waves.
 310 Whatever the mechanism is, our result shows that the time scale for such process to energize
 311 electrons to 1–2 MeV is slow, > 70 hr.

312

313 **4.3 The radial dependence of the radiation belt electrons on the solar wind density and** 314 **velocity**

315 The effects of the n_{sw} and V_{sw} on the radiation belt electrons have a dependence on the
 316 radial distance or L^* (e.g., *Baker et al., 2019a; Tang et al., 2017a; Turner et al., 2019; Zhao et al.,*
 317 *2017; W. Li et al., 2014).* In order to show this, PSD data are binned from $L^* = 3$ to 6.5 into 7 bins
 318 with bin width = 0.5. The data coverage for the electrons with $\mu = 725\text{--}875$ MeV G^{-1} and $K =$
 319 $0.09\text{--}0.13 R_E G^{-0.5}$ is poor for $L^* < 3$ and $L^* > 6.5$. Figure 5 shows $\text{corr}(n_{sw} \rightarrow \text{PSD})$ as a function
 320 of L^* . It shows that the correlation is near 0 at $L^* = 3\text{--}3.5$, but slowly decreases with increasing
 321 L^* . Except for $L^* = 3\text{--}3.5$ ($n = 8435$, Figure 5a), the correlations are significant ($p < 0.01$) at the
 322 minimum τ ($\tau = 15, 16, 17, 17, 17, 13$ hr), $r = (-0.086, -0.17, -0.27, -0.31, -0.34, -0.50)$, ($n =$
 323 $8,302, 11,481, 17,7891, 27,060, 6,236, 528$) for panels (b–g), respectively. The number of points
 324 in $L^* = 6\text{--}6.5$ (Figure 5g) is the fewest, which results in a noisier correlation. However, as
 325 discussed in the Sections 1, 4.1, and 4.2, the correlation may be inaccurate because n_{sw} negatively
 326 correlates with V_{sw} (Figure 2c) and the system is nonlinear (Wing et al., 2016). Hence, we calculate
 327 $\text{CMI}(n_{sw} \rightarrow \text{PSD} | V_{sw})$ for the PSD data in the same bins. The results are plotted in Figure 6. The
 328 figure shows that the effect of n_{sw} on PSD is at the noise level at $L^* = 3\text{--}4.5$, is significant at $L^* =$
 329 $5\text{--}6$, and back to the noise level at $L^* = 6\text{--}6.5$. However, the result for $L^* = 6\text{--}6.5$ is considered

330 not reliable because of the small number of points ($n = 528$). The response lag times based on the
331 first peak are $\tau = 9, 10, \text{ and } 7 \text{ hr}$ ($n = 16,629, 25,238, \text{ and } 5865$; significance = 17, 42, and 5 σ) at
332 $L^* = 4.5\text{--}5, 5\text{--}5.5, \text{ and } 5.5\text{--}6$, respectively. Notice that the response lag times are quite different
333 in Figures 5 and 6.

334 For completeness, we examine the effect of P_{dyn} on the PSD. Figure 7 plots $\text{CMI}(P_{dyn} \rightarrow$
335 $\text{PSD} | V_{sw})$ as a function of L^* in the same format as Figure 6. It shows that the effect of P_{dyn} on
336 PSD is similar to that of n_{sw} , as expected. The largest effect of P_{dyn} on electron PSD can be found
337 at $L^* = 4.5\text{--}6$. (significance = 32, 53, 17 σ for $L^* = 4.5\text{--}5, 5\text{--}5.5, \text{ and } 5.5\text{--}6$), respectively. The
338 number of points in each bin in Figure 6 is the same as that in Figure 7. Taken together, Figures
339 6 and 7 suggest that the magnetopause shadowing is effective only at $L^* = 4.5\text{--}6$. At $L^* = 6\text{--}6.5$,
340 there is a high variability of PSD and the bin has fewest number of points and hence the result is
341 inconclusive.

342 Moreover, the significances are higher for the first peak in Figure 7 panels d–f than their
343 counterparts for $\text{CMI}(n_{sw} \rightarrow \text{PSD} | V_{sw})$ in Figure 6 panels d–f, suggesting that the real causal
344 parameter for the magnetopause shadowing is P_{dyn} rather than n_{sw} . However, the opposite is true
345 for the secondary peak. This would suggest that the secondary peak may be more causally related
346 to n_{sw} (or its proxy) than P_{dyn} .

347 We perform the same analysis with V_{sw} and electron PSD. Figure 8 shows $\text{corr}(V_{sw} \rightarrow$
348 $\text{PSD})$ as a function of L^* in the same format as Figure 5. The correlations are all significant at $p <$
349 0.01 at the maximum τ ($\tau = 40\text{--}120, 30\text{--}120, 38, 30, 37, 45, 30\text{--}90 \text{ hr}$), ($r = 0.14, 0.27, 0.42, 0.57,$
350 $0.62, 0.64, 0.70$) for $L^* = 3\text{--}3.5, 3.5\text{--}4, 4\text{--}4.5, 4.5\text{--}5, 5\text{--}5.5, 5.5\text{--}6, \text{ and } 6\text{--}6.5$, respectively. Baker
351 et al. (2019a) also found higher correlation with increasing L ($r = 0.32, 0.51, \text{ and } 0.61$ for $L = 3.5,$
352 $4.5, \text{ and } 5.5$, respectively). For comparison, Figure 9 plots $\text{CMI}(V_{sw} \rightarrow \text{PSD} | n_{sw})$ as a function of

353 L^* in the same format as Figure 6. The number of points in each bin is the same as that in Figure
354 6. Figure 9 shows that the CMI is at the noise level at $L^* = 3-3.5$ (panel a), unlike its counterpart
355 in Figure 8a. At $L^* = 3.5-4.5$, the CMI has a broad peak from $\tau \sim 50-100$ hr (or larger for the case
356 $L^* = 3.5-4$) and the peaks are significant (peak significance = 18 and 46 σ for $L^* = 3.5-4$ and 4-
357 4.5), respectively. At $L^* = 4.5-6$, the CMI peaks are narrower (peak $\tau = 40, 46, 57$ hr; significance
358 = 236, 399, and 100 σ), respectively. Interestingly, at $\tau = 6-6.5$, the peak broadens again but
359 remains significant (peak significance = 19 σ). To help visualize the evolution of the CMI, red
360 dashed vertical lines at $\tau = 40$ hr is drawn in Figure 9.

361 The radiation belt electron response lag times as a function of L^* is further examined in
362 Figure 10. The figure shows the normalized i_{tr} for each L^* bin (the blue curve subtracted by the
363 solid green curve in Figure 9). The orange and yellow color correspond roughly to the top 20% of
364 i_{tr} in each L^* bin. At $L^* = 4.5-5.5$, response lag time peaks around $\tau = 35-50$ hours, which is
365 consistent or close to the previously reported time scale of 2 days to accelerate electrons to 1-2
366 MeV (*Paulikas and Blake, 1979; Reeves et al., 2011; Li et al., 2001; Wing et al., 2016*). At higher
367 L^* , $L^* = 5.5-6$, the peak broadens and shifts to larger τ , $\tau = 45-65$ hr. At $L^* = 6-6.5$, the peak is
368 even broader at $\tau = 40-100$ hr. At lower L^* , $L^* = 4-4.5$ and $3.5-4$, one can also see successive
369 broadening of the peak as the peak shifts to larger τ , $\tau = 35-55$ hr and $\tau = 45-60$ hr, respectively.

370 Our result is consistent with local acceleration where the peak of the electron acceleration
371 region is located at $L^* = 4.5-5.5$, from where electrons diffuse outward and inward (Section 5.3).
372 This scenario would be consistent with the *O'Brien et al. (2003)* study that found the peak of the
373 1.5 MeV electron microburst precipitation is located at $L = 4.5$. It would also be consistent with
374 the *Green and Kivelson (2004)* study that found evidence for local acceleration near $L^* = 5$. More
375 recently, in the RBSP era, *Tang et al. (2017a)* found that the peak flux of 1 MeV electrons is

376 located mostly at $L \sim 4-5$ in 74 storm events and they also found evidence for local acceleration.
377 *Boyd et al. (2018)* found the peak PSD is located mostly at $L^* = 4.5 - 5.5$ in 80 storm events. They
378 concluded that 70 out of 80 events show evidence of local acceleration based on the PSD vs. L^*
379 spectra. These results are consistent with our interpretation of Figures 9 and 10 that the L^* band
380 with the information peak at the smallest τ corresponds to the local acceleration region. The
381 shifting of the peak to a larger τ at higher or lower L^* suggests outward or inward diffusion,
382 respectively.

383 However, there is also evidence that suggests localized acceleration in tandem with
384 outward or inward diffusion originating from $L^* = 4.5-5.5$ (e.g., Allison and Shprits, 2020). For
385 example, at $L^* = 4-4.5$, one can see that the i_{lr} starts increasing at $\tau = 25$ hr, very much about the
386 same time i_{lr} increases at $L^* = 4.5-5.5$ hr, but the significance is lower (Figure 9). This may
387 suggest that the whistler mode chorus waves are also present at $L^* = 4-4.5$ and not all 1-2 MeV
388 electrons are transported from $L^* = 4.5-5.5$. The same dynamics can be seen at the outermost L^* ,
389 $L^* = 6-6.5$.

390 The radial diffusion time scale can be estimated from the peak τ at each L^* band. In Figure
391 10, the peak τ increases from ~ 40 hr at $L^* = 4.5-5.5$ to ~ 60 hr at $L^* = 5.5-6$, suggesting outward
392 diffusion time scale of 40 hr per R_E . The diffusion time scale of 40 hr (or about 2 days) per R_E can
393 be compared with the theoretical estimate of 1-6 days that is attributed to ULF waves at $L^* = 6$
394 (e.g., *Elkington et al., 2003*).

395

396 **4.4 The dependence of the radiation belt electrons on the magnetospheric state**

397 So far we have analyzed the dependence of the radiation belt electron PSD on the solar
398 wind drivers, specifically V_{sw} , n_{sw} , and P_{dyn} . However, the radiation belt electrons depend not just

399 on the external (solar wind) drivers but also the internal state of the magnetosphere (e.g., *Reeves*
400 *et al.*, 1998; *Baker et al.*, 2019a; *Lyatsky and Khazanov*, 2008b; *Borovsky and Denton*, 2014; *Tang*
401 *et al.*, 2017b; *Borovsky*, 2017; *Zhao et al.*, 2017). In order to determine how the radiation belt
402 electrons depend on the internal state of the magnetosphere, we examine the relationships of the
403 electron PSD with AL and SYM-H indices. SYM-H index gives a measure of the strength of the
404 ring current and storm (*Iyemori*, 1990) while AL gives a measure of the strength of the westward
405 auroral electrojets and substorm (*Davis and Sugiura*, 1966). SYM-H is similar to Disturbance
406 Storm Time (Dst) index (*Dessler and Parker*, 1959), except that SYM-H index is defined to have
407 a one minute time resolution whereas Dst index has one hour resolution. Both SYM-H (proxy for
408 storms) and AL (proxy for substorms) can be associated with plasma injections to the inner
409 magnetosphere, which can enhance the whistler mode chorus waves and provide the seed
410 population for the local acceleration (*Katus et al.*, 2013; *Wing et al.*, 2014).

411 Figure 11a plots $\text{corr}(\text{AL} \rightarrow \text{PSD})$, which shows that AL negatively correlates with electron
412 PSD with a minimum $\tau \sim 53$ hr ($n = 70,125$, $r = -0.33$, $p < 0.01$). Note that a smaller (more
413 negative) AL corresponds to a more intense substorm and larger auroral electrojets. Figure 11b
414 plots $\text{corr}(V_{sw} \rightarrow \text{PSD})$ (same as Figure 1a). Figure 11c plots $\text{corr}(V_{sw} \rightarrow \text{AL})$, which shows that
415 the auroral electrojet response to V_{sw} is fairly quick $\tau = 0$ hr (< 30 min) ($n = 82,995$, $r = -0.40$, $p <$
416 0.01). Similar correlation was obtained by *Smirnov et al.* (2020). Given the positive correlation
417 of V_{sw} and electron PSD, and the negative correlation of V_{sw} and AL, one may ask the question
418 whether the negative correlation between AL and electron PSD may just simply be coincidental or
419 whether AL can independently affect PSD. Figure 11d plots $\text{CMI}(\text{AL} \rightarrow \text{PSD} | V_{sw})$, which shows
420 that the radiation belt electrons still have strong dependence on AL even after the effect of V_{sw} has
421 been removed. The CMI peaks at $\tau \sim 50\text{--}80$ hr (significance = 58σ , $n = 64,564$), suggesting that

422 perhaps the time scale to accelerate electrons to 1–2 MeV energy range from the time of substorm
423 onset or substorm particle injection is about 50–80 hr. This time scale is an ensemble average for
424 all L^* . To help visualize the comparison of Figures 11a and 11d, a dashed vertical red line is
425 drawn at $\tau = 53$ hr (the minimum of $\text{corr}(\text{AL} \rightarrow \text{PSD})$). It shows that removing the effect of V_{sw} ,
426 shifts the peak to the right (to a larger τ) by a little bit (~ 10 hr).

427 Figure 12 displays the normalized i_{tr} as a function of L^* and τ where $i_{tr} = \text{CMI}(\text{AL} \rightarrow \text{PSD} |$
428 $V_{sw}) - \text{mean noise}$ in the same format as Figure 10. The i_{tr} is at the noise level at $L^* = 3-3.5$ ($n =$
429 6409). At $L^* = 6-6.5$, there is a high variability in PSD and the bin has the fewest number of
430 points ($n = 216$) and hence the result is unclear and not shown. The region with the largest
431 significance is $L^* = 4.5-5$ and $5-5.5$ with peak $\tau = 40-80$ and $45-85$ hr and peak significance =
432 33 and 38σ ($n = 13,825$ and $20,527$) respectively. The peak shifts to larger τ , $\tau = 75-100$ hr, at
433 $L^* = 5.5-6$ ($n = 4686$, peak significance = 18σ), suggesting outward diffusion from $L^* = 4.5-5.5$.
434 At $L^* = 4-4.5$, the peak is broad, $\tau = 35-80$ hr ($n = 8802$; peak significance = 19σ). It is not clear
435 what causes this broad peak. Because the peak starts at the same time or even earlier than at
436 $L^*=4.5-5.5$, it may suggest the whistler wave activity is present nearly simultaneously from $L^* =$
437 $4-5.5$. However, the peak seems to decay slowly suggesting perhaps inward diffusion or longer
438 lasting wave activity at $L^* = 4-4.5$. At $L^* = 3.5-4$, the peak is broad at $\tau = 60-110$ hr, but the
439 peak significance is relatively small ($n = 6379$, peak significance = 9σ), which would be consistent
440 with inward diffusion from higher L^* .

441 *Iles et al.* (2006) examined a substorm event and found that peak PSD for electrons > 0.8
442 MeV is located at $L^* = 4.3-5.5$, which is close to the L^* band with the largest CMI significance,
443 $L^* = 4.5-5.5$. They also found evidence of local acceleration and radial diffusion.

444 We perform similar analysis with SYM-H. Radiation belt electrons have been found to

445 show great variabilities during storms (e.g., *Reeves et al.*, 2003; *Turner et al.*, 2019; *Baker et al.*,
 446 2019a). Figure 13 is similar to Figure 11, except that it is for SYM-H instead of AL index. Figure
 447 13a plots $\text{corr}(\text{SYM-H} \rightarrow \text{PSD})$, which shows that SYM-H negatively correlates with electron
 448 PSD with a minimum at $\tau \sim 40$ hr ($n = 91,589$, $r = -0.35$, $p < 0.01$) while Figure 13b plots $\text{corr}(\text{SYM-H} \rightarrow \text{PSD})$
 449 ($V_{sw} \rightarrow \text{PSD}$) (same as Figure 11b). V_{sw} negatively correlates with SYM-H and the correlation has
 450 a minimum at $\tau = 2-4$ hr ($n = 91,589$, $r = -0.35$, $p < 0.01$) (Figure 13c), suggesting that the ring
 451 current response to V_{sw} has a lag time of about 2–4 hr. Similar correlation was obtained in previous
 452 studies (e.g., *Maggiolo et al.*, 2017). Figures 13 a–c pose the same dilemma as Figures 11 a–c do
 453 for AL. That is, given the positive correlation of V_{sw} and electron PSD and the negative correlation
 454 of V_{sw} and SYM-H, one may ask whether the negative correlation of SYM-H and PSD could just
 455 simply be coincidental or whether SYM-H provides additional information about PSD. Figure
 456 13d plots $\text{CMI}(\text{SYM-H} \rightarrow \text{PSD} | V_{sw})$, which shows that SYM-H indeed provides additional
 457 information to electron PSD even after the effect of V_{sw} has been removed. The CMI peaks at $\tau \sim$
 458 30–70 hr ($n = 84,729$, significance = 109σ), suggesting that perhaps the time scale to accelerate
 459 electrons to 1–2 MeV energy range from the time of ring current enhancement is about 30–70 hr.
 460 However, the effect of SYM-H has a dependence on radial distance, as discussed next.

461 Figure 14 plots i_{tr} as a function of L^* where $i_{tr} = \text{CMI}(\text{SYM-H} \rightarrow \text{PSD} | V_{sw}) - \text{mean noise}$
 462 in the same format as Figure 12. The figure suggests a complicated relationship between SYM-H
 463 and radiation belt electrons. At $L^* = 6-6.5$, i_{tr} is at the noise level, which can be attributed to high
 464 PSD variabilities as well as small number of points ($n = 336$). Studies found that storms can
 465 increase, decrease, or have little effect on radiation belt electron fluxes at geosynchronous orbit
 466 (e.g., *O'Brien et al.*, 2001; *Reeves et al.*, 2003). An increase in SYM-H (or ring current) would
 467 decrease magnetospheric $|B|$ by greater proportion with increasing L^* because magnetospheric $|B|$

468 decreases with r^{-3} (e.g., *Turner et al.*, 2012). The effect of the reduction in $|B|$ would be a decrease
469 in PSD due to the outward transport because of the third adiabatic invariant. This Dst or SYM-H
470 effect would counter the effect of the PSD enhancement due to the storm plasma injection and the
471 ensuing local acceleration.

472 The highest peak significance can be found at $L^* = 5 - 5.5$ (peak $\tau = 20-55$ hr, significance
473 $= 79\sigma$, $n = 27,060$). The peak shifts to higher τ at higher L^* , suggesting outward diffusion. At L^*
474 $= 5.5-6$, the peak can be found at $\tau = 60-75$ hr ($n = 6236$, peak significance $= 26 \sigma$). At $L^* = 4-$
475 4.5 and $4.5-5$, the i_{tr} peaks at $\tau = 30-60$ and $30-75$ hr ($n = 11,495$ and $17,924$; peak significance
476 $= 38$ and 47σ , respectively). The large i_{tr} at $L^* = 4-5$ would be roughly consistent with *Tang et*
477 *al.* (2017a), which found that the peak flux of 1 MeV electron at $L = 4-5$ in 74 storm events and
478 with *Green and Kivelson* (2004), which found local acceleration at $L^* = 5$.

479 At $L^* = 3.5-4$, the peak is very broad at $\tau = 20-120$ hr or even higher ($n = 8317$, peak
480 significance $= 23 \sigma$). It is not clear what causes such a broad peak. The response at $\tau < 30$ hr
481 suggests that the 1-2 MeV electrons at this time could not have originated from higher L^* shell.
482 Thus, it may suggest the presence of wave activity at this L^* band. On the other hand, the response
483 at $\tau > 80$ hr, may suggest inward diffusion from higher L^* shell or long-lasting wave activity. At
484 $L^* = 3-3.5$, the CMI peaks at $\tau = 110-120$ hr or even higher ($n = 8435$, peak significance $= 14$).
485 The analysis stops at $\tau = 120$ hr. The large τ may suggest slow diffusion from outer L^* shell. The
486 slow diffusion at small L^* would be consistent with the expected radial diffusion time scale that
487 increases with decreasing $|B|$ and L^* , but this needs to be investigated further. It is worth noting
488 that out of all the parameters that we have examined, only SYM-H can provide information about
489 radiation belt electron PSD at $L^* = 3-3.5$ albeit only a small amount. The CMI at $L^* = 3-3.5$ and
490 $\tau < 100$ hr is low, which is consistent with *Turner et al.* (2019) study that found storms have little

491 effect on 1–2 MeV electrons at $L < 3.5$ (see their Figure 2), but apparently at $\tau > 100$ hr, the storm
492 effect is significant but only moderately.

493 The complicated response of the radiation belt to SYM-H or storm can be attributed to
494 multiple factors. The general response of the storm plasma injection is PSD enhancement through
495 local acceleration. However, this effect is countered by the Dst (SYM-H) effect due to the ring
496 current enhancement, which would cause outward electron drift and a decrease PSD because of
497 the the third adiabatic invariant. This Dst (SYM-H) effect is stronger with increasing L^* because
498 at $|B|$ decreases with r^3 . Moreover, different type storms can affect radiation belt electrons
499 differently. For example, *Turner et al* (2019) reported that full coronal mass ejection (CME)
500 storms cause MeV electron enhancements at $L < \sim 5$ while stream interaction region (SIR) storms
501 cause enhancements at $L > \sim 4.5$. CME sheaths and CME ejecta can cause depletions throughout
502 the outer radiation belt.

503

504 **4.5 The rankings of solar wind and magnetospheric parameters by the information transfer** 505 **to the radiation belt electrons**

506 In the previous sections, we calculate the dependence of the PSD on V_{sw} , n_{sw} , P_{dyn} , AL, and
507 SYM-H. V_{sw} transfers the most information to the PSD by significantly larger amount than any
508 other solar wind variables. In this section, we calculate the CMI from other solar wind parameters
509 to the PSD, given V_{sw} . Specifically, we calculate $CMI(x \rightarrow PSD | V_{sw})$ where $x = IMF |B|, B_z < 0,$
510 $B_z > 0, B_y, E_{sw},$ and $\sigma(IMF B)$.

511 Table 1 ranks these parameters based on the information transfer to the radiation belt
512 electron PSD, given V_{sw} for $L^* = 3 - 6.5$. The information transfer is calculated as $i_{tr_max} =$
513 maximum of (CMI – mean noise). The information transfer from V_{sw} to the PSD is calculated

514 from $CMI(V_{sw} \rightarrow PSD | n_{sw})$. It shows the dominance of V_{sw} in terms of information transfer to the
515 PSD. SYM-H, which is ranked second, transfers only about a quarter as much information to the
516 PSD. In Table 1, if the response lag time has a broad peak, τ is reported as having a range of
517 values. Table 1 shows that the radiation belt electron response lag time to the solar wind and
518 magnetospheric parameters fall into two categories. The electron response with a small τ ($\tau < 15$
519 hr) is a decrease in PSD (electron loss) while the response at large τ ($\tau > 40$ hr) is an enhancement
520 in PSD.

521 Zhao et al. (2017) correlated PSD with solar wind (V_{sw} , n_{sw} , P_{dyn}) and magnetospheric
522 parameters (SYM-H, AL) and found that AL has the best correlation with PSD with $t = 2-5$ days
523 for $\mu > 700$ MeV G^{-1} . However, their study differs from the present study in two key aspects: (1)
524 their study used daily resolution data; (2) more importantly, they did not remove the effect of V_{sw}
525 from AL, SYM-H, and other parameters. The second point is particularly consequential because
526 AL negatively correlates with V_{sw} (Figure 11c) and some of the good correlation between AL and
527 PSD can be partially attributed to the good correlation between V_{sw} and PSD.

528 Many of the parameters, namely IMF $|B|$, IMF $B_z < 0$, IMF B_y , n_{sw} , and P_{dyn} , produce dual
529 response modes in the radiation belt electrons. At small τ ($\tau < 15$ hr), the response is a decrease
530 in PSD or electron loss while at large τ ($\tau > 30$ hr), the response is an enhancement in PSD. For
531 these parameters, the ranking is based on the mode that has the higher i_{tr_max} . The response to IMF
532 $|B|$ has roughly the same i_{tr_max} at small and large τ , although Table 1 lists the response to the large
533 τ . The response to IMF $|B|$, IMF $B_z < 0$, and IMF B_y at $\tau < 15$ hr is electron loss and is mainly due
534 to their correlations with n_{sw} . If the effect of n_{sw} is removed, this peak will diminish or disappear.
535 An example for IMF $B_z > 0$ is illustrated in Figures 4e and 4f.

536 The ranking presented in Table 1 can be useful for modeling radiation belt electrons. The

537 table may help modelers decide which parameters need to be considered as inputs to their models.

538

539 **5. Discussion and conclusion**

540 **5.1 Untangling the solar wind and magnetospheric drivers**

541 An important factor that is often ignored and underappreciated in many solar wind-
542 magnetosphere interaction studies is that many solar wind parameters positively or negatively
543 correlate with one another, which may introduce complications and ambiguities in the causal-effect
544 interpretation of the data. In the present study, we use conditional mutual information, CMI, to
545 untangle the effects of the solar wind and magnetospheric drivers of the radiation belt electrons
546 PSD having $\mu = 725\text{--}875 \text{ MeV G}^{-1}$ and $K = 0.09\text{--}0.13 \text{ R}_E \text{ G}^{-0.5}$ (average energy $\sim 1.6 \text{ MeV}$).

547 The radiation belt electron response time lags to V_{sw} , n_{sw} , AL, and SYM-H obtained from
548 correlational analysis differ from those obtained from CMIs that have removed the effect of the
549 V_{sw} or n_{sw} as summarized in Table 2 (from Figures 2, 11, and 13). For the purpose of facilitating
550 a more precise comparison, Table 2 lists only the peak τ even if the peak may be broad whereas
551 Table 1 lists a range of τ , if the peak is broad. The response lag times obtained by CMIs are
552 deemed more accurate because the effect of V_{sw} or n_{sw} has been removed. For example, $\text{CMI}(n_{sw}$
553 $\rightarrow \text{PSD} | V_{sw})$ peaks at $t = 7\text{--}11 \text{ hr}$ whereas $\text{corr}(n_{sw} \rightarrow \text{PSD})$ has a minimum at $\tau = 15 \text{ hr}$ (*Lyatsky*
554 *and Khazanov, 2008a*). The smaller τ is deemed a more accurate time scale for magnetopause
555 shadowing, which physically makes sense and is consistent with observations (e.g., *Turner et*
556 *al., 2014a; Xiang et al., 2017; 2018; Turner and Ukhorskiy, 2020*). The shift in the peak CMI
557 depends on the conditional variable z in the $\text{CMI}(x \rightarrow y | z)$. If the (linear and nonlinear) correlation
558 of z with y is smaller than that between x and y , then removing the effect of z would shift the peak
559 to a larger value and vice versa.

560 The response of the radiation belt electrons to n_{sw} has dual mode. At small τ , n_{sw} negatively
561 correlates with the electron PSD with a peak response time at $\tau = 7\text{--}11$ hr, which can be attributed
562 to the magnetopause shadowing effect. However, at large τ ($\tau > 80$ hr), n_{sw} positively correlates
563 with the electron PSD as shown in Figures 2e and 3. It is not clear what causes this positive
564 correlation. n_{sw} may be a proxy for another solar wind parameter. n_{sw} negatively correlates with
565 IMF $B_z < 0$, which may be the real driver. However, n_{sw} and IMF $B_z < 0$ may be both proxies for
566 another parameter. For example, an increase in n_{sw} is sometimes accompanied by n_{sw} fluctuations,
567 which can drive ULF waves in the magnetosphere and accelerate electrons (e.g., *Kepko and Viall,*
568 *2019, Ukhorskiy et al., 2005*). Interestingly, the secondary peak in $\text{CMI}(n_{sw} \rightarrow \text{PSD} | V_{sw})$ at $L^* =$
569 $4.5\text{--}5.5$ (Figures 6d and 6e) is more prominent and significant than its counterpart in $\text{CMI}(P_{dyn} \rightarrow$
570 $\text{PSD} | V_{sw})$ (Figures 7d and 7e), suggesting that the driver for the secondary peak may be more
571 related to n_{sw} rather than P_{dyn} . Whichever parameter drives the electron acceleration, the result
572 suggests a rather slow process for electron acceleration, $\tau > 80$ hr. This will be investigated in our
573 follow up study.

574

575 **5.2 The radial dependences of the radiation belt electrons**

576 The responses of radiation belt electrons to V_{sw} , n_{sw} , P_{dyn} , AL, and SYM-H have radial
577 dependence. The data coverage for the electrons with $\mu = 725\text{--}875$ MeV G^{-1} and $K = 0.09\text{--}0.13$
578 $R_E \text{G}^{-0.5}$ is poor for $L^* < 3$ and $L^* > 6.5$. Hence, the present study does not consider these L^*
579 ranges. The effect of n_{sw} and P_{dyn} on the radiation belt electron PSD appear to be significant only
580 at $L^* = 4.5\text{--}6$ and insignificant at $L^* = 3\text{--}4.5$. This suggests that the magnetopause shadowing is
581 effective mostly at $L^* = 4.5\text{--}6$. At $L^* = 6\text{--}6.5$, there is a high variability in PSD and the bin has
582 the fewest number of points ($n = 336$) and hence the result is deemed unreliable. In contrast, the

583 effect of V_{sw} on the electron PSD appears to be significant at a larger range of L^* , $L^* = 3.5$ to 6.5 .

584 An increase in n_{sw} or P_{dyn} compresses the magnetosphere leading to the electron loss at
585 high L^* , e.g., $L^* > 7$. However, ULF waves generated throughout the magnetosphere due to the
586 compression would redistribute the loss to lower L^* . Our result shows that the electron loss can
587 be seen at $L^* = 4.5$ – 6 , consistent with understanding from observations and simulations (*Turner*
588 *et al.* 2012, 2014a; *Xiang et al.* 2017; 2018; *Turner and Ukhorskiy*, 2020). At higher L^* , the noise
589 in the $CMI(n_{sw} \rightarrow PSD | V_{sw})$ is higher, which can be attributed to higher variability of the PSD.
590 For example, the PSD initially decreases due to the magnetopause compression and then increase
591 because of the outward diffusion (*Turner et al.*, 2012; *Shprits et al.*, 2006). Our result differs from
592 Zhao et al. (2017) that found that P_{dyn} negatively correlates with PSD only at a small range of L^*
593 band near 6 (see their Figure 4c).

594 The radiation belt electrons also have strong dependences on the internal state of the
595 magnetosphere. In the present study, this is explored and exemplified with AL and SYM-H, which
596 can be used as proxies for magnetospheric state. However, the dependences on AL and SYM-H
597 vary with radial distance or L^* . The dependence of the radiation belt electrons on AL is significant
598 at $L^* = 4$ – 6 while the dependence on SYM-H is significant at $L^* = 3$ – 6 . The response of the
599 radiation belt electrons to AL and SYM-H peak at $\tau = 40$ – 80 and $\tau = 20$ – 60 hr, respectively. These
600 lag times are averaged for all L^* . AL and SYM-H are proxies for substorms and storms,
601 respectively. Substorm and storm injections can increase the temperature anisotropy in the inner
602 magnetosphere, which are important for local acceleration mechanism discussed in Section 5.3.
603 However, it is not clear why there is a large difference between the response lag times to AL and
604 that to SYM-H. This difference in response lag times are also seen in the $\text{corr}(\text{AL} \rightarrow \text{PSD})$ and
605 $\text{corr}(\text{SYM-H} \rightarrow \text{PSD})$ in Zhao et al. (2017), but their peak τ are smaller, which can be attributed,

606 at least partly, to their usage of daily resolution data and their correlations did not remove the effect
607 of V_{sw} .

608

609 **5.3 Implications to electron acceleration mechanism and transport**

610 One of the fundamental questions in radiation belt physics is how the electrons are
611 accelerated to relativistic energies (> 1 MeV). There have been many proposed mechanisms, but
612 most tend to fall into two categories: (1) local acceleration and (2) radial transport (see review in
613 Friedel et al., 2002).

614 In the local acceleration mechanism, substorms or storms transport low energy electrons (a
615 few to tens of keVs) from the plasma sheet into the inner magnetosphere, which are often referred
616 to as the source population (e.g., *Baker et al.*, 1996; *Tang et al.*, 2017a; *Boyd et al.*, 2016). The
617 temperature anisotropy in the source population leads to the growth of the VLF whistler mode
618 chorus waves (e.g., *Meredith et al.*, 2001; *W. Li et al.*, 2009). Substorms and storms also transport
619 high energy electrons (a few tens to hundreds keVs) electrons from the plasma sheet into the inner
620 magnetosphere, which are commonly referred to as seed population. Then, the chorus waves
621 interact with the seed electrons and energize them to relativistic energies (e.g., *Summers et al.*,
622 1998; 2002; *Horne et al.*, 2005; *Omura et al.*, 2007; Thorne, 2010; Reeves et al., 2013; *W. Li et*
623 *al.*, 2014).

624 In the radial transport acceleration mechanism, electrons at larger L^* get accelerated as
625 they move inward to the inner magnetosphere through interactions with ULF waves (e.g., *Baker*
626 *et al.*, 1998; *Li and Temerin*, 2001; *Li et al.*, 2005; *Ukhorskiy et al.*, 2005; *Mathie and Mann*, 2000;
627 *Elkington et al.*, 1999; *Kepko and Viall*, 2019). These ULF waves can be associated with high V_{sw}
628 and Kelvin-Helmholtz Instability (KHI) or n_{sw} or P_{dyn} fluctuations (e.g., *Johnson et al.*, 2014;

629 *Engebretson et al.*, 1998; *Vennerstrøm*, 1999; *Claudepierre et al.*, 2010; *Takahashi and Ukhorskiy*,
630 2007; *Liu et al.*, 2010).

631 The result of $\text{CMI}(V_{sw} \rightarrow \text{PSD} | n_{sw})$ as a function of L^* (Figures 9 and 10) can be interpreted
632 in terms of local acceleration mechanism. Figure 10 suggests that the radiation belt electrons at
633 $L^* = 4.5\text{--}5.5$ have the shortest response lag time with peak $\tau = 35\text{--}50$ hr and the highest
634 significance. The response lag time is larger and broader at higher L^* , $\tau = 45\text{--}65$ hr ($L^* = 5.5\text{--}6$),
635 $\tau = 40\text{--}100$ hr ($L^* = 6\text{--}6.5$), and at lower L^* , $\tau = 35\text{--}55$ hr ($L^* = 4\text{--}4.5$) and $\tau = 45\text{--}60$ hr ($L^* =$
636 $3.5\text{--}4$). This would suggest that local acceleration peaks at $L^* = 4.5\text{--}5.5$ and then subsequent
637 outward and inward diffusion spreads enhancements from this L^* band. Previous studies also
638 found evidence for local acceleration at this L^* band by examining the MeV PSD or electron fluxes
639 as a function of radial distance (*Green and Kivelson*, 2004; *Boyd et al.*, 2018; *Tang et al.*, 2017a)
640 or microburst MeV electron precipitation (*O'Brien et al.*, 2003). At $L^* = 4\text{--}4.5$, there is evidence
641 of weak local acceleration. Its i_{tr} starts increasing at about the same time as that for $L^* = 4.5\text{--}5.5$,
642 but its significance is lower than that for $L^* = 4.5\text{--}5.5$.

643 Our finding differs from previous studies that attributed the good correlation between V_{sw}
644 and PSD to ULF waves and radial transport (e.g., *Rostoker et al.*, 1998; *Elkington et al.*, 1999;
645 *Mathie and Mann*, 2000; *Zhao et al.*, 2017).

646 The radial diffusion time scale can be estimated by considering the peak τ of each L^* bin
647 in Figure 10. It is found that the outward diffusion from $L^* = 5$ to 6 is about 2 days per.

648 The result of $\text{CMI}(\text{AL} \rightarrow \text{PSD} | V_{sw})$ can also be interpreted as consistent with local
649 acceleration at $L^* = 4\text{--}5.5$ and inward and outward diffusion to lower and higher L^* , respectively.
650 This may not be too surprising because the link between V_{sw} and PSD involves substorm injections.

651 However, the radiation belt electron response lag time appears more complicated for

652 CMI(SYM-H \rightarrow PSD| V_{sw}) (Figure 14). The peak τ is most significant and smallest at $L^* = 5-5.5$
653 suggesting local acceleration peaks at this L^* band. There is evidence for inward and outward
654 diffusion from this L^* band. However, there is also evidence for local acceleration at smaller L^* .
655 The complication may stem from the competing processes that would increase and decrease PSD
656 and electron fluxes. A decrease of SYM-H would indicate increase in the ring current and the
657 intensity of storms. The general response to storm plasma injections would be an increase in
658 whistler mode chorus waves and electron acceleration, leading to an increase in PSD. However,
659 storm would increase the ring current, which would reduce $|B|$. This would cause outward
660 diffusion and reduction of PSD as the electrons would attempt to conserve the third adiabatic
661 invariant (*Turner et al.*, 2012). This Dst or SYM-H effect would be stronger with increasing radial
662 distance. This could be a contributing factor in the high noise and variability seen in $L^* = 6-6.5$.
663 Studies have shown that the radiation belt electron response at the outermost L^* band can
664 sometimes be enhancement, depletion, or no change (*O'Brien et al.*, 2001; *Reeves et al.*, 2003).
665 These competing processes may contribute to this variability in the radiation belt response. Also,
666 different types of storms would affect different L^* differently (*Turner et al.*, 2019).

667

668 **5.4 Ranking of the solar wind and magnetospheric drivers**

669 We rank the solar wind and magnetospheric parameters based on the information transfer
670 to the radiation belt electron PSD. This ranking can be useful for modelers who would like to
671 develop models that input solar wind and magnetospheric parameters and predict radiation belt
672 electrons having energies 1–2 MeV. This is shown in Table 1. The table shows that V_{sw} transfers
673 the most information to the radiation belt electrons and hence should be considered an important,
674 if not the most important, input parameter to radiation belt models. However, SYM-H can also be

675 an important input parameter for models for two reasons: (1) SYM-H transfers the second most
676 information to the radiation belt electrons; and (2) Out of a long list of parameters (V_{sw} , n_{sw} , P_{dyn} ,
677 AL, SYM-H), only SYM-H has information the radiation belt electrons at $L^* = 3-3.5$ albeit only
678 a small amount of information. SYM-H can play a crucial role for models that predict the radiation
679 belt electrons at $L^* = 3-3.5$.

680

681

682 *Acknowledgments.* The solar wind, SYM-H, and AL dataset were obtained from NASA
683 OMNIweb <https://omniweb.gsfc.nasa.gov/>. All the derived data products in this paper are
684 available upon request by email (simon.wing@jhuapl.edu). All RBSP-ECT data are publicly
685 available at the website <http://www.rbsp-ect.lanl.gov>. Simon Wing acknowledges support of
686 NASA Van Allen Probe Contract NNN16AA09T and NASA Grants NNX16AQ87G,
687 80NSSC20K0704, 80NSSC19K0843, 80NSSC19K0822, 80NSSC20K0188, 80NSSC20K1279,
688 and 80NSSC20K1271. Drew Turner is thankful for funding from NASA grants 80NSSC19K0280
689 and 80NSSC18K1377. This work has benefitted from discussions within the International Space
690 Science Institute (ISSI) Team # 455 “Complex Systems Perspectives Pertaining to the Research
691 of the Near-Earth Electromagnetic Environment.”

692

693

694

695

References

696 Allison, H.J., Shprits, Y. Y. (2020), Local heating of radiation belt electrons to ultra-relativistic
697 energies. *Nat Commun* **11**, 4533, <https://doi.org/10.1038/s41467-020-18053-z>

698 Alves, L.R., Souza, V.M., Jauer, P.R. *et al.* The Role of Solar Wind Structures in the Generation
699 of ULF Waves in the Inner Magnetosphere. *Sol Phys* **292**, 92 (2017).
700 <https://doi.org/10.1007/s11207-017-1113-4>

701 Baker, D. N., R. L. McPherron, T. E. Cayton, and R. W. Klebesadel (1990), Linear prediction
702 filter analysis of relativistic electron properties at 6.6 R_E , *J. Geophys. Res.*, 95(A9),15133–
703 15140, doi:[10.1029/JA095iA09p15133](https://doi.org/10.1029/JA095iA09p15133).

704 Baker, D. N., Pulkkinen, T. I., Angelopoulos, V., Baumjohann, W., and McPherron, R.
705 L. (1996), Neutral line model of substorms: Past results and present view, *J. Geophys.*
706 *Res.*, 101(A6), 12975– 13010, doi:[10.1029/95JA03753](https://doi.org/10.1029/95JA03753).

707 Baker, D. N., X Li, J. B Blake, S. Kanekal (1998), Strong electron acceleration in the Earth's
708 magnetosphere, *Adv. Space Res.*, 21, 609-613, doi:10.1016/S0273-1177(97)00970-8.

709 Baker, D. N., et al. (2012), The Relativistic Electron-Proton Telescope (REPT) Instrument on
710 Board the Radiation Belt Storm Probes (RBSP) Spacecraft: Characterization of Earth's
711 Radiation Belt High-Energy Particle Populations, *Space Sci. Rev.*, doi:10.1007/s11214-012-
712 9950-9.

713 Baker, D.N., Erickson, P.J., Fennell, J.F. *et al.* Space Weather Effects in the Earth's Radiation
714 Belts. *Space Sci Rev* **214**, 17 (2018). <https://doi.org/10.1007/s11214-017-0452-7>

715 Baker, D. N., Hoxie, V., Zhao, H., Jaynes, A. N., Kanekal, S., Li, X., & Elkington,
716 S. (2019a). Multiyear measurements of radiation belt electrons: Acceleration, transport, and

717 loss. *Journal of Geophysical Research: Space*
718 *Physics*, 124, 2588–2602. <https://doi.org/10.1029/2018JA026259>

719 Baker, D. N., Zhao, H., Li, X., Kanekal, S. G., Jaynes, A. N., Kress, B. T., et al. (2019b).
720 Comparison of Van Allen Probes Energetic Electron Data with corresponding GOES-15
721 Measurements: 2012–2018. *Journal of Geophysical Research: Space Physics*, 124,
722 <https://doi.org/10.1029/2019JA027331>

723 Balasis, G., Daglis, I. A., Papadimitriou, C., Kalimeri, M., Anastasiadis, A., and Eftaxias,
724 K. (2008), Dynamical complexity in D_{st} time series using non-extensive Tsallis
725 entropy, *Geophys. Res. Lett.*, 35, L14102, doi:[10.1029/2008GL034743](https://doi.org/10.1029/2008GL034743).

726 Balasis, G., Daglis, I. A., Papadimitriou, C., Kalimeri, M., Anastasiadis, A., and Eftaxias,
727 K. (2009), Investigating dynamical complexity in the magnetosphere using various entropy
728 measures, *J. Geophys. Res.*, 114, A00D06, doi:[10.1029/2008JA014035](https://doi.org/10.1029/2008JA014035).

729 Balasis, G., C. Papadimitriou, I. A. Daglis, A. Anastasiadis, L. Athanasopoulou, and K. Eftaxias
730 (2011), Signatures of discrete scale invariance in D_{st} time series, *Geophys. Res. Lett.*, 38,
731 L13103, doi: [10.1029/2011GL048019](https://doi.org/10.1029/2011GL048019).

732 Balasis, G.; Donner, R.V.; Potirakis, S.M.; Runge, J.; Papadimitriou, C.; Daglis, I.A.; Eftaxias, K.;
733 Kurths (2013), J. Statistical mechanics and information-theoretic perspectives on complexity
734 in the Earth system. *Entropy*, 15, 4844–4888, doi:[10.3390/e15114844](https://doi.org/10.3390/e15114844).

735 Balikhin, M. A., R. J. Boynton, S. A. Billings, M. Gedalin, N. Ganushkina, D. Coca, and H.
736 Wei (2010), Data based quest for solar wind-magnetosphere coupling function, *Geophys.*
737 *Res. Lett.*, 37, L24107, doi:[10.1029/2010GL045733](https://doi.org/10.1029/2010GL045733).

738 Balikhin, M. A., R. J. Boynton, S. N. Walker, J. E. Borovsky, S. A. Billings, and H. L.
739 Wei(2011), Using the NARMAX approach to model the evolution of energetic electrons
740 fluxes at geostationary orbit, *Geophys. Res. Lett.*, 38, L18105, doi:[10.1029/2011GL048980](https://doi.org/10.1029/2011GL048980).

741 Birn, J., and E. W. Hones Jr. (1981), Three-dimensional computer modeling of dynamic
742 reconnection in the geomagnetic tail, *J. Geophys. Res.*, 86, 6802–6808,
743 doi:10.1029/JA086iA08p06802.

744 Birn, J., M. F. Thomsen, J. E. Borovsky, G. D. Reeves, D. J. McComas, and R. D. Belian (1997),
745 Characteristic plasma properties during disper- sionless substorm injections at
746 geosynchronous orbit, *J. Geophys. Res.*, 102, 2309–2324.

747 Birn, J., M. Hesse, and K. Schindler, Entropy conservation in simulations of magnetic
748 reconnection (2006b), *Phys. Of Plasma*, 13, 092117, doi: 10.1063/1.2349440.

749 Blake, J.B., Carranza, P.A., Claudepierre, S.G. *et al.* *The Magnetic Electron Ion*
750 *Spectrometer* (MagEIS) Instruments Aboard the Radiation Belt Storm Probes (RBSP)
751 *Spacecraft. Space Sci Rev* **179**, 383–421 (2013). [https://doi.org/10.1007/s11214-013-9991-](https://doi.org/10.1007/s11214-013-9991-8)
752 [8](https://doi.org/10.1007/s11214-013-9991-8)

753 Borovsky, J. E. (2012), The velocity and magnetic field fluctuations of the solar wind at 1 AU:
754 Statistical analysis of Fourier spectra and correlations with plasma properties, *J. Geophys.*
755 *Res.*, 117, A05104, doi:[10.1029/2011JA017499](https://doi.org/10.1029/2011JA017499).

756 Borovsky, J. E., and Denton, M. H. (2014), Exploring the cross correlations and autocorrelations
757 of the ULF indices and incorporating the ULF indices into the systems science of the solar
758 wind-driven magnetosphere, *J. Geophys. Res. Space Physics*, 119, 4307– 4334,
759 doi:[10.1002/2014JA019876](https://doi.org/10.1002/2014JA019876).

760 Borovsky, J. E. (2016), The plasma structure of coronal hole solar wind: Origins and evolution, *J.*
761 *Geophys. Res. Space Physics*, 121, 5055– 5087, doi:[10.1002/2016JA022686](https://doi.org/10.1002/2016JA022686).

762 Borovsky, J. E. (2017). Time-integral correlations of multiple variables with the relativistic-
763 electron flux at geosynchronous orbit: The strong roles of substorm-injected electrons and
764 the ion plasma sheet. *Journal of Geophysical Research: Space*
765 *Physics*, 122, 11,961– 11,990. <https://doi.org/10.1002/2017JA024476>

766 Borovsky, J. E. (2018), On the origins of the intercorrelations between solar wind
767 variables. *Journal of Geophysical Research: Space*
768 *Physics*, 123, 20– 29. <https://doi.org/10.1002/2017JA024650>

769 Borovsky, J. E. (2020), What magnetospheric and ionospheric researchers should know about the
770 solar wind, *J. Atmos. Sol. Phys.*, 204, 105271, <https://doi.org/10.1016/j.jastp.2020.105271>.

771 Boyd, A. J., Spence, H. E., Claudepierre, S. G., Fennell, J. F., Blake, J. B., Baker, D. N., Reeves,
772 G. D., and Turner, D. L. (2014), Quantifying the radiation belt seed population in the March
773 17, 2013 electron acceleration event, *Geophys. Res. Lett.*, 41, 2275– 2281,
774 doi:[10.1002/2014GL059626](https://doi.org/10.1002/2014GL059626).

775 Boyd, A. J., Spence, H. E., Huang, C.-L., Reeves, G. D., Baker, D. N., Turner, D. L., Claudepierre,
776 S. G., Fennell, J. F., Blake, J. B., and Shprits, Y. Y. (2016), Statistical properties of the
777 radiation belt seed population, *J. Geophys. Res. Space Physics*, 121, 7636– 7646,
778 doi:[10.1002/2016JA022652](https://doi.org/10.1002/2016JA022652).

779 Boyd, A. J., Turner, D. L., Reeves, G. D., Spence, H. E., Baker, D. N., & Blake, J. B. (2018). What
780 causes radiation belt enhancements: A survey of the Van Allen Probes Era. *Geophysical*
781 *Research Letters*, 45, 5253– 5259. <https://doi.org/10.1029/2018GL077699>

782 Boyd, A. J., Spence, H. E., Reeves, G. D., Funsten, H. O., Skoug, R. M., Larsen, B. A., et al.
783 (2021). RBSP-ECT combined pitch angle resolved electron flux data product. *Journal of*
784 *Geophysical Research: Space Physics*, 126,
785 e2020JA028637. <https://doi.org/10.1029/2020JA028637>

786 Claudepierre, S. G., M. K. Hudson, W. Lotko, J. G. Lyon, and R. E. Denton (2010), Solar wind
787 driving of magnetospheric ULF waves: Field line resonances driven by dynamic pressure
788 fluctuations, *J. Geophys. Res.*, 115, A11202, doi:[10.1029/2010JA015399](https://doi.org/10.1029/2010JA015399).

789 Consolini, G., R. Tozzi, and P. De Michelis (2009), Complexity in the sunspot cycle, *A&A* 506,
790 1381–1391, DOI: 10.1051/0004-6361/200811074

791 Davis, T. N., and Sugiura, M. (1966), Auroral electrojet activity index *AE* and its universal time
792 variations, *J. Geophys. Res.*, 71(3), 785– 801, doi:[10.1029/JZ071i003p00785](https://doi.org/10.1029/JZ071i003p00785).

793 Darbellay, G. A., and I. Vajda (1999), Estimation of the Information by an Adaptive Partitioning
794 of the Observations Space, *IEEE Transactions on Information Theory*, 45, 1315–1321.

795 De Michelis, P., G. Consolini, M. Materassi, and R. Tozzi (2011), An information theory
796 approach to the storm-substorm relationship, *J. Geophys. Res.*, 116, A08225,
797 doi:[10.1029/2011JA016535](https://doi.org/10.1029/2011JA016535).

798 De Michelis, P.; Tozzi, R.; Consolini, G. (2017), Statistical analysis of geomagnetic field intensity
799 differences between ASM and VFM instruments onboard Swarm constellation. *Earth*
800 *Planets Space*, 69, 24, doi:10.1186/s40623-016-0583-1.

801 Dessler, A., and E. Parker (1959), Hydromagnetic theory of geomagnetic storms, *J. Geophys.*
802 *Res.*, 64(12), 2239–2252, doi:[10.1029/JZ064i012p02239](https://doi.org/10.1029/JZ064i012p02239).

803 Elkington, S. R., M. K. Hudson, and A. A. Chan (1999), Acceleration of relativistic electrons via
804 drift-resonant interaction with toroidal-mode Pc-5 ULF oscillations, *Geophys. Res. Lett.*, 26,
805 3273.

806 Elkington, S. R., Hudson, M. K., and Chan, A. A. (2003), Resonant acceleration and diffusion of
807 outer zone electrons in an asymmetric geomagnetic field, *J. Geophys. Res.*, 108, 1116,
808 doi:[10.1029/2001JA009202](https://doi.org/10.1029/2001JA009202)

809 Engebretson, M., K.-H. Glassmeier, M. Stellmacher, W. J. Hughes, and H. Lühr (1998), The
810 dependence of high-latitude PcS wave power on solar wind velocity and on the phase of
811 high-speed solar wind streams, *J. Geophys. Res.*, 103(A11), 26271–26283,
812 doi:[10.1029/97JA03143](https://doi.org/10.1029/97JA03143).

813 Friedel, R. H. W., G. D. Reeves, and T. Obara (2002), Relativistic electron dy-
814 namics in the inner magnetosphere—A review, *J. Atmos. Sol. Terr. Phys.*, 64, 265.

815 Green, J. C., and M. G. Kivelson (2004), Relativistic electrons in the outer radiation belt:
816 Differentiating between acceleration mechanisms, *J. Geophys. Res.*, 109, A03213,
817 doi:[10.1029/2003JA010153](https://doi.org/10.1029/2003JA010153).

818 Horne, R. B., R. M. Thorne, S. A. Glauert, J. M. Albert, N. P. Meredith, and R. R. Anderson
819 (2005), Timescale for radiation belt electron acceleration by whistler mode chorus waves, *J.*
820 *Geophys. Res.*, 110, A03225, doi:[10.1029/2004JA010811](https://doi.org/10.1029/2004JA010811)

821 Hudson, M. K., Kress, B. T., Mueller, H.-R., Zastrow, J. A., & Blake, J. B. (2008). Relationship
822 of the Van Allen radiation belts to solar wind drivers. *Journal of Atmospheric and Solar-*
823 *Terrestrial Physics*, 70, 708–729. <https://doi.org/10.1016/j.jastp.2007.11.003>

824 Hundhausen, A. J., S. J. Bame, J. R. Asbridge, and S. J. Sydoriak (1970), Solar wind proton
825 properties: Vela 3 observations from July 1965 to June 1967, *J. Geophys.*
826 *Res.*, 75(25),4643–4657, doi:[10.1029/JA075i025p04643](https://doi.org/10.1029/JA075i025p04643)

827 Iles, R. H. A., Meredith, N. P., Fazakerley, A. N., and Horne, R. B. (2006), Phase space density
828 analysis of the outer radiation belt energetic electron dynamics, *J. Geophys. Res.*, 111,
829 A03204, doi:[10.1029/2005JA011206](https://doi.org/10.1029/2005JA011206).

830 Iyemori, T. (1990), Storm-time magnetospheric currents inferred from mid-latitude geomagnetic
831 field variations, *J. Geomag. Geoelectr.*, 42, 1249–1265.

832 Jaynes, A. N., et al. (2015), Source and seed populations for relativistic electrons: Their roles in
833 radiation belt changes, *J. Geophys. Res. Space Physics*, 120, doi:10.1002/2015JA021234.

834 Jaynes, A. N., Ali, A. F., Elkington, S. R., Malaspina, D. M., Baker, D. N., Li, X., et al.
835 (2018). Fast diffusion of ultrarelativistic electrons in the outer radiation belt: 17 March 2015
836 storm event. *Geophysical Research Letters*, 45, 10,874– 10,882.
837 <https://doi.org/10.1029/2018GL079786>

838 Johnson, J. R., and S. Wing (2005), A solar cycle dependence of nonlinearity in magnetospheric
839 activity, *J. Geophys. Res.*, 110, A04211, doi:[10.1029/2004JA010638](https://doi.org/10.1029/2004JA010638).

840 Johnson, J. R., and S. Wing (2014), External versus internal triggering of substorms: An
841 information-theoretical approach, *Geophys. Res. Lett.*, 41, 5748–5754,
842 doi:[10.1002/2014GL060928](https://doi.org/10.1002/2014GL060928).

843 Johnson, J. R., S. Wing, and P. A. Delamere (2014), Kelvin Helmholtz Instability in Planetary
844 Magnetospheres, *Space Sci. Rev.*, 184, 1 – 31, doi:10.1007/s11214-014-0085-z.

845 Johnson, J. R., Wing, S., and Camporeale, E. (2018), Transfer entropy and cumulant-based cost as
846 measures of nonlinear causal relationships in space plasmas: applications to D_{st} , *Ann.*
847 *Geophys.*, 36, 945-952, <https://doi.org/10.5194/angeo-36-945-2018>

848 Katus, R. M., Liemohn, M. W., Gallagher, D. L., Ridley, A., and Zou, S. (2013), Evidence for
849 potential and inductive convection during intense geomagnetic events using normalized
850 superposed epoch analysis, *J. Geophys. Res. Space Physics*, 118, 181–191,
851 doi:[10.1029/2012JA017915](https://doi.org/10.1029/2012JA017915).

852 Kellerman, A. C., and Y. Y. Shprits (2012), On the influence of solar wind conditions on the outer-
853 electron radiation belt, *J. Geophys. Res.*, 117, A05217, doi:[10.1029/2011JA017253](https://doi.org/10.1029/2011JA017253).

854 Kepko, L., & Viall, N. M. (2019). The source, significance, and magnetospheric impact of periodic
855 density structures within stream interaction regions. *Journal of Geophysical Research: Space*
856 *Physics*, 124, 7722–7743. <https://doi.org/10.1029/2019JA026962>

857 Lejosne, S., Kollmann, P. Radiation Belt Radial Diffusion at Earth and Beyond. *Space Sci*
858 *Rev* **216**, 19 (2020). <https://doi.org/10.1007/s11214-020-0642-6>

859 Li, W. (1990), Mutual Information Functions Versus Correlation Functions, *J. Stat. Phys.*, 60, 823–
860 837.

861 Li, W., Thorne, R. M., Angelopoulos, V., Bonnell, J. W., McFadden, J. P., Carlson, C.
862 W., LeContel, O., Roux, A., Glassmeier, K. H., and Auster, H. U. (2009), Evaluation of
863 whistler-mode chorus intensification on the nightside during an injection event observed on
864 the THEMIS spacecraft, *J. Geophys. Res.*, 114, A00C14, doi:[10.1029/2008JA013554](https://doi.org/10.1029/2008JA013554).

865 Li, W., et al. (2014), Radiation belt electron acceleration by chorus waves during the 17 March
866 2013 storm, *J. Geophys. Res. Space Physics*, 119, 4681–4693, doi:[10.1002/2014JA019945](https://doi.org/10.1002/2014JA019945).

867 Li, X., and M. A. Temerin (2001), The electron radiation belt, *Space Sci. Rev.*, 95, 569 - 580.

868 Li, X., M. Temerin, D. Baker, G. Reeves, and D. Larson (2001), Quantitative prediction of
869 radiation belt electrons at geostationary orbit based on solar wind measurements, *Geophys.*
870 *Res. Lett.*, **28**(9), 1887–1890.

871 Li, X., D. N. Baker, M. Temerin, G. Reeves, R. Friedel, and C. Shen (2005), Energetic electrons,
872 50 keV to 6 MeV, at geosynchronous orbit: Their responses to solar wind variations, *Space*
873 *Weather*, 3, S04001, doi:[10.1029/2004SW000105](https://doi.org/10.1029/2004SW000105).

874 Li, X., Barker, A. B., Baker, D. N., Tu, W. C., Sarris, T. E., Selesnick, R. S., Friedel, R., and Shen,
875 C. (2009), Modeling the deep penetration of outer belt electrons during the “Halloween”
876 magnetic storm in 2003, *Space Weather*, 7, S02004, doi:[10.1029/2008SW000418](https://doi.org/10.1029/2008SW000418).

877 Liu, W., Sarris, T. E., Li, X., Ergun, R., Angelopoulos, V., Bonnell, J., and Glassmeier, K.
878 H. (2010), Solar wind influence on Pc4 and Pc5 ULF wave activity in the inner
879 magnetosphere, *J. Geophys. Res.*, 115, A12201, doi:[10.1029/2010JA015299](https://doi.org/10.1029/2010JA015299).

880 Lui, A. T. Y. (1991), Extended consideration of a synthesis model for magnetospheric substorms,
881 in *Magnetospheric Substorms*, pp. 43-60, *Geophys. Monog.*, 64, edited by J. R. Kan, T. A.
882 Potemra, S. Kokubun, and T. Ijima, AGU, Washington D.C.,

883 Lyatsky, W., and G. V. Khazanov (2008a), Effect of solar wind density on relativistic electrons at
884 geosynchronous orbit, *Geophys. Res. Lett.*, 35, L03109, doi:[10.1029/2007GL032524](https://doi.org/10.1029/2007GL032524).

885 Lyatsky, W., and G. V. Khazanov (2008b), Effect of geomagnetic disturbances and solar wind
886 density on relativistic electrons at geostationary orbit, *J. Geophys. Res.*, 113, A08224,
887 doi:[10.1029/2008JA013048](https://doi.org/10.1029/2008JA013048).

888 Lyons, L. R. (1995), A new theory for magnetospheric substorms, *J. Geophys. Res.*, 100, 19,069–
889 19,082, doi:[10.1029/95JA01344](https://doi.org/10.1029/95JA01344).

890 Lyons, L. R., G. T. Blanchard, J. C. Samson, R. P. Lepping, T. Yamamoto, and T. Moretto (1997),
891 Coordinated observations demonstrating external substorm triggering, *J. Geophys. Res.*,
892 102, 27,039–27,052, doi:10.1029/97JA02639.

893 Maggiolo, R., Hamrin, M., De Keyser, J., Pitkänen, T., Cessateur, G., Gunell, H., & Maes, L.
894 (2017). The delayed time response of geomagnetic activity to the solar wind. *Journal of*
895 *Geophysical Research: Space Physics*, 122, 11,109– 11,127.
896 <https://doi.org/10.1002/2016JA023793>

897 Mann, I. R., Ozeke, L. G., Murphy, K. R., Claudepierre, S. G., Turner, D. L., Baker, D. N., et al.
898 (2016). Explaining the dynamics of the ultra- relativistic third Van Allen Radiation belt.
899 *Nature Physics*, 12(10), 978–983. <https://doi.org/10.1038/NPHYS3799>

900 March, T. K., Chapman, S. C., and Dendy, R. O. (2005), Mutual information between
901 geomagnetic indices and the solar wind as seen by WIND: Implications for propagation time
902 estimates, *Geophys. Res. Lett.*, 32, L04101, doi:[10.1029/2004GL021677](https://doi.org/10.1029/2004GL021677).

903 Mathie, R. A., & Mann, I. R. (2000). A correlation between extended intervals of ULF wave power
904 and stormtime geosynchronous relativistic electron flux enhancements. *Geophysical*
905 *Research Letters*, 27(20), 3261–3264. <https://doi.org/10.1029/2000gl003822>

906 McPherron, R. (1991), Physical processes producing magnetospheric substorms and magnetic
907 storms, in *Geomagnetism*, edited by J. Jacobs, pp. 593–739, Academic Press, London, U. K.

908 McPherron, R. L., Terasawa, and A. Nishida (1986), Solar wind triggering of substorm
909 expansion onset, *J. Geomagn. Geoelectr.*, 38(11), 1089–1108, doi:10.5636/jgg.38.1089.

910 Manshour,P., Balasis,G.; Consolini, G.; Papadimitriou, C., Paluš, M. (2021), Causality and
911 Information Transfer Between the Solar Wind and the Magnetosphere–Ionosphere System.
912 *Entropy*, 23, 390. <https://doi.org/10.3390/e23040390>

913 Materassi, M., L. Ciruolo, G. Consolini, and N. Smith (2011), Predictive Space Weather: An
914 information theory approach, *Adv. Space Res.*, 47, 877–885, doi:10/106/j.asr.2010.10.026.

915 Mathie, R. A., and I. R. Mann (2000), A correlation between extended intervals of ULF wave
916 power and storm-time geosynchronous relativistic electron flux enhancements, *Geophys.*
917 *Res. Lett.*, 27, 3621–3264, doi:[10.1029/2000GL003822](https://doi.org/10.1029/2000GL003822).

918 Mathie, R. A., and I. R. Mann (2001), On the solar wind control of Pc5 ULF pulsation power at
919 mid-latitudes: Implications for MeV electron acceleration in the outer radiation belt, *J.*
920 *Geophys. Res.*, 106(A12), 29783–29796, doi:[10.1029/2001JA000002](https://doi.org/10.1029/2001JA000002).

921 Mauk, B. H., N. J. Fox, S. G. Kanekal, R. L. Kessel, D. G. Sibeck, and A. Ukhorskiy (2013),
922 Science objectives and rationale for the radiation belt storm probes mission, *Space Science*
923 *Review*, 179(1-4), 3–27, doi:10.1007/s11214-012-9908-y.

924 Meredith, N. P., Horne, R. B., and Anderson, R. R. (2001), Substorm dependence of chorus
925 amplitudes: Implications for the acceleration of electrons to relativistic energies, *J. Geophys.*
926 *Res.*, 106(A7), 13165– 13178, doi:[10.1029/2000JA900156](https://doi.org/10.1029/2000JA900156).

927 Miyoshi, Y., R. Kataoka, Y. Kasahara, A. Kumamoto, T. Nagai, and M. F. Thomsen (2013), High-
928 speed solar wind with southward interplanetary magnetic field causes relativistic electron
929 flux enhancement of the outer radiation belt via enhanced condition of whistler waves,
930 *Geophys. Res. Lett.*, 40, doi:10.1002/grl.50916.

931 Newell, P. T., K. Liou, J.W. Gjerloev, T. Sotirelis, S. Wing, E.J. Mitchell (2016), Substorm
932 probabilities are best predicted from solar wind speed, *J. Atmos. Sol. Terr. Phys.*, 146, 28-
933 37, doi:10.1016/j.jastp.2016.04.019.

934 O'Brien, T. P., McPherron, R. L., Sornette, D., Reeves, G. D., Friedel, R., and Singer, H.
935 J. (2001), Which magnetic storms produce relativistic electrons at geosynchronous orbit?, *J.*
936 *Geophys. Res.*, 106(A8), 15533– 15544, doi:[10.1029/2001JA000052](https://doi.org/10.1029/2001JA000052).

937 O'Brien, T. P., Lorentzen, K. R., Mann, I. R., Meredith, N. P., Blake, J. B., Fennell, J. F., Looper,
938 M. D., Milling, D. K., and Anderson, R. R. (2003), Energization of relativistic electrons in
939 the presence of ULF power and MeV microbursts: Evidence for dual ULF and VLF
940 acceleration, *J. Geophys. Res.*, 108, 1329, doi:10.1029/2002JA009784, A8.

941 Onsager, T. G., J. C. Green, G. D. Reeves, and H. J. Singer (2007), Solar wind and magnetospheric
942 conditions leading to the abrupt loss of outer radiation belt electrons, *J. Geophys. Res.*, 112,
943 A01202, doi:[10.1029/2006JA011708](https://doi.org/10.1029/2006JA011708).

944 Omura, Y., N. Furuya, and D. Summers (2007), Relativistic turning acceleration of resonant
945 electrons by coherent whistler mode waves in a dipole magnetic field, *J. Geophys. Res.*, 112,
946 A06236, doi:[10.1029/2006JA012243](https://doi.org/10.1029/2006JA012243)

947 Papadimitriou, Constantinos; Balasis, Georgios; Boutsis, Adamantia Z.; Daglis, Ioannis A.;
948 Giannakis, Omiros; Anastasiadis, Anastasios; Michelis, Paola D.; Consolini, Giuseppe.
949 (2020), Dynamical Complexity of the 2015 St. Patrick's Day Magnetic Storm at Swarm
950 Altitudes Using Entropy Measures, *Entropy*, 22, 5, 574, <https://doi.org/10.3390/e22050574>

951 Paulikas, G. A., and J. B. Blake (1979), Effects of the solar wind on magnetospheric dynamics:
952 Energetic electrons at the synchronous orbit, in *Quantitative Modeling of Magnetospheric*
953 *Processes, Geophys. Monogr. Ser.*, Vol 21, pp. 180-202, AGU, Washington D.C.

954 Pinto, V. A., Kim, H.-J., Lyons, L. R., & Bortnik, J. (2018). Interplanetary parameters leading to
955 relativistic electron enhancement and persistent depletion events at geosynchronous orbit

956 and potential for prediction. *Journal of Geophysical Research: Space*
957 *Physics*, 123, 1134–1145. <https://doi.org/10.1002/2017JA024902>

958 Prichard, D., and J. Theiler (1995), Generalized redundancies for time series analysis, *Physica D:*
959 *Non-linear Phenomena*, 84, 476–493, doi:10.1016/0167-2789(95)00041-2.

960 Reeves, G. D. (1998), Relativistic electrons and magnetic storms: 1992–1995, *Geophys. Res. Lett.*,
961 25, 1817–1820, doi:10.1029/98GL01398.

962 Reeves, G. D., McAdams, K. L., Friedel, R. H. W., and O'Brien, T. P. (2003), Acceleration and
963 loss of relativistic electrons during geomagnetic storms, *Geophys. Res. Lett.*, 30, 1529,
964 doi:[10.1029/2002GL016513](https://doi.org/10.1029/2002GL016513)

965 Reeves, G. D. (2007), Radiation Belt Storm Probes: A New Mission for Space Weather
966 Forecasting. *Space Weather*, 5: n/a. doi:10.1029/2007SW000341

967 Reeves, G. D., S. K. Morley, R. H. W. Friedel, M. G. Henderson, T. E. Cayton, G. Cunningham, J.
968 B. Blake, R. A. Christensen, and D. Thomsen (2011), On the relationship between
969 relativistic electron flux and solar wind velocity: Paulikas and Blake revisited, *J. Geophys.*
970 *Res.*, 116, A02213, doi:[10.1029/2010JA015735](https://doi.org/10.1029/2010JA015735).

971 Reeves, G., S. Morley, and G. Cunningham (2013), Long-term variations in solar wind velocity
972 and radiation belt electrons, *J. Geophys. Res. Space Physics*, 118, 1040–1048,
973 doi:[10.1002/jgra.50126](https://doi.org/10.1002/jgra.50126).

974 Rigler, E. J., M. Wiltberger, and D. N. Baker (2007), Radiation belt electrons respond to multiple
975 solar wind inputs, *J. Geophys. Res.*, 112, A06208, doi:[10.1029/2006JA012181](https://doi.org/10.1029/2006JA012181)

976 Roederer, J. G. (1970), *Dynamics of Geomagnetically Trapped Radiation*, Springer, New York,
977 <https://doi.org/10.1007/978-3-642-49300-3>

978 Rostoker, G. (1983), Triggering of expansive phase intensifications of magnetospheric substorms

979 by northward turnings of the interplanetary magnetic field, *J. Geophys. Res.*, 88, 6981–6993,
980 doi:10.1029/JA088iA09p06981.

981 Rostoker, G., S. Skone, and D. N. Baker (1998), On the origin of relativistic electrons in the
982 magnetosphere associated with some geomagnetic storms, *Geophys. Res. Lett.*, **25**, 3701–
983 3704, doi:[10.1029/98GL02801](https://doi.org/10.1029/98GL02801).

984 Runge, J., Balasis, G., Daglis, I.A. *et al.* Common solar wind drivers behind magnetic storm–
985 magnetospheric substorm dependency. *Sci Rep* **8**, 16987 (2018).
986 <https://doi.org/10.1038/s41598-018-35250-5>

987 Schulz, M., and L.J. Lanzerotti (1974) , Particle Diffusion in the Radiation Belts, Springer, Berlin,
988 1974, <https://doi.org/10.1007/978-3-642-65675-0>

989 Simms, L. E., V. Pilipenko, M. J. Engebretson, G. D. Reeves, A. J. Smith, and M.
990 Clilverd (2014), Prediction of relativistic electron flux at geostationary orbit following
991 storms: Multiple regression analysis, *J. Geophys. Res. Space Physics*, 119, 7297–7318,
992 doi:[10.1002/2014JA019955](https://doi.org/10.1002/2014JA019955).

993 Shprits, Y. Y., R. M. Thorne, R. Friedel, G. D. Reeves, J. Fennell, D. N. Baker, and S. G.
994 Kanekal (2006), Outward radial diffusion driven by losses at magnetopause, *J. Geophys.*
995 *Res.*, 111, A11214, doi:[10.1029/2006JA011657](https://doi.org/10.1029/2006JA011657)

996 Shprits, Y. Y., D. A. Subbotin, N. P. Meredith, S. R. Elkington (2008), Review of modeling of
997 losses and sources of relativistic electrons in the outer radiation belt II: Local acceleration
998 and loss, *J. Atmos. Sol. Terr. Phys.*, 70, 1694-1713, doi:10.1016/j.jastp.2008.06.014.

999 Shprits, Y. Y., D. Subbotin, and B. Ni (2009), Evolution of electron fluxes in the outer radiation
1000 belt computed with the VERB code, *J. Geophys. Res.*, 114, A11209,
1001 doi:[10.1029/2008JA013784](https://doi.org/10.1029/2008JA013784).

1002 Smirnov, A. G., Berrendorf, M., Shprits, Y. Y., Kronberg, E. A., Allison, H. J., Aseev, N. A., et
1003 al. (2020). Medium energy electron flux in earth's outer radiation belt (MERLIN): A
1004 machine learning model. *Space Weather*, 18,
1005 e2020SW002532. <https://doi.org/10.1029/2020SW002532>

1006 Snelling, Jesse M., Jay R. Johnson, Jake Willard, Yosia Nurhan, Jonathan Homan, and Simon
1007 Wing (2020), Information Theoretical Approach to Understanding Flare Waiting Times, *The*
1008 *Astrophysical Journal*, 899, 148, <http://dx.doi.org/10.3847/1538-4357/aba7b9>

1009 Spence, H.E., Reeves, G.D., Baker, D.N. et al. (2013), Science Goals and Overview of the
1010 Radiation Belt Storm Probes (RBSP) Energetic Particle, Composition, and Thermal Plasma
1011 (ECT) Suite on NASA's Van Allen Probes Mission. *Space Sci Rev* 179, 311–336,
1012 <https://doi.org/10.1007/s11214-013-0007-5>

1013 Stumpo, Mirko; Consolini, Giuseppe; Alberti, Tommaso; Quattrocioni, Virgilio. 2020.
1014 "Measuring Information Coupling between the Solar Wind and the Magnetosphere–
1015 Ionosphere System" *Entropy* 22, no. 3: 276. <https://doi.org/10.3390/e22030276>

1016 Summers, D., R. M. Thorne, and F. Xiao (1998), Relativistic theory of wave-particle resonant
1017 diffusion with application to electron acceleration in the magnetosphere, *J. Geophys.*
1018 *Res.*, 103(A9), 20487–20500, doi:[10.1029/98JA01740](https://doi.org/10.1029/98JA01740).

1019 Summers, D., Ma, C., Meredith, N. P., Horne, R. B., Thorne, R. M., Heynderickx, D.,
1020 and Anderson, R. R. (2002), Model of the energization of outer-zone electrons by whistler-
1021 mode chorus during the October 9, 1990 geomagnetic storm, *Geophys. Res. Lett.*, 29(24),
1022 2174, doi:[10.1029/2002GL016039](https://doi.org/10.1029/2002GL016039).

1023 Summers, D., B. Ni, and N. P. Meredith (2007), Timescales for radiation belt electron acceleration
1024 and loss due to resonant wave-particle interactions: 1. Theory, *J. Geophys. Res.*, 112,
1025 A04206, doi:[10.1029/2006JA011801](https://doi.org/10.1029/2006JA011801).

1026 Tang, C. L., Wang, Y. X., Ni, B., Zhang, J.-C., Reeves, G. D., Su, Z. P., Baker, D. N., Spence, H.
1027 E., Funsten, H. O., and Blake, J. B. (2017a), Radiation belt seed population and its
1028 association with the relativistic electron dynamics: A statistical study, *J. Geophys. Res.*
1029 *Space Physics*, 122, 5261– 5276, doi:[10.1002/2017JA023905](https://doi.org/10.1002/2017JA023905).

1030 Tang, C. L., Wang, Y. X., Ni, B., Su, Z. P., Reeves, G. D., Zhang, J.-C., Baker, D. N., Spence, H.
1031 E., Funsten, H. O., and Blake, J. B. (2017b), The effects of magnetospheric processes on

1032 relativistic electron dynamics in the Earth's outer radiation belt, *J. Geophys. Res. Space*
1033 *Physics*, 122, 9952–9968, doi:[10.1002/2017JA024407](https://doi.org/10.1002/2017JA024407).

1034 Takahashi, K., and Ukhorskiy, A. Y. (2007), Solar wind control of Pc5 pulsation power at
1035 geosynchronous orbit, *J. Geophys. Res.*, 112, A11205, doi:[10.1029/2007JA012483](https://doi.org/10.1029/2007JA012483).

1036 Thorne, R. M. (2010), Radiation belt dynamics: The importance of wave-particle
1037 interactions, *Geophys. Res. Lett.*, 37, L22107, doi:[10.1029/2010GL044990](https://doi.org/10.1029/2010GL044990)

1038 Thorne, R. M., et al. (2013), Rapid local acceleration of relativistic radiation-belt electrons by
1039 magnetospheric chorus, *Nature*, 504(7480), 411–414, doi:10.1038/nature12889.

1040 Tsonis, A. A. (2001), Probing the linearity and nonlinearity in the transitions of the atmospheric
1041 circulation, *Nonlinear Processes in Geophysics*, 8, 341–345.

1042 Turner, D. L., and Li, X. (2008), Quantitative forecast of relativistic electron flux at
1043 geosynchronous orbit based on low-energy electron flux, *Space Weather*, 6, S05005,
1044 doi:10.1029/2007SW000354.

1045 Turner, D. L., and X. Li (2011), Using spacecraft measurements ahead of Earth in the Parker spiral
1046 to improve terrestrial space weather forecasts, *Space Weather*, 9, S01002,
1047 doi:10.1029/2010SW000627

1048 Turner, D. L., Y. Shprits, M. Hartinger, and V. Angelopoulos (2012), Explaining sudden losses
1049 of outer radiation belt electrons during geomagnetic storms, *Nat. Phys.*, 8, 208–212,
1050 doi:10.1038/nphys2185.

1051 Turner, D. L., et al. (2014a), On the cause and extent of outer radiation belt losses during the 30
1052 September 2012 dropout event, *J. Geophys. Res. Space Physics*, 119, 1530–1540,
1053 doi:[10.1002/2013JA019446](https://doi.org/10.1002/2013JA019446).

1054 Turner, D. L., et al. (2014b), Competing source and loss mechanisms due to wave-particle
1055 interactions in Earth's outer radiation belt during the 30 September to 3 October 2012
1056 geomagnetic storm, *J. Geophys. Res. Space Physics*, 119, 1960–1979,
1057 doi:[10.1002/2014JA019770](https://doi.org/10.1002/2014JA019770).

1058 Turner, D. L., Kilpua, E. K. J., Hietala, H., Claudepierre, S. G., O'Brien, T. P., Fennell, J. F., et al.
1059 (2019). The response of Earth's electron radiation belts to geomagnetic storms: Statistics
1060 from the Van Allen Probes era including effects from different storm drivers. Journal of
1061 Geophysical Research: Space Physics, 124, 1013– 1034.
1062 <https://doi.org/10.1029/2018JA026066>

1063 Turner, D. L., and A. Y. Ukhorskiy (2020), Chapter 1 - Outer radiation belt losses by
1064 magnetopause incursions and outward radial transport: new insight and outstanding
1065 questions from the Van Allen Probes era, in The dynamic loss of Earth's radiation belts eds.
1066 Allison N. Jaynes and Maria E. Usanova, Elsevier (2020), pp. 1–20, ISBN 9780128133712,
1067 <https://doi.org/10.1016/B978-0-12-813371-2.00001-9>

1068 Ukhorskiy, A. Y., M. I. Sitnov, A. S. Sharma, B. J. Anderson, S. Ohtani, and A. T. Y. Lui (2004),
1069 Data-derived forecasting model for relativistic electron intensity at geosynchronous
1070 orbit, Geophys. Res. Lett., 31, L09806, doi:[10.1029/2004GL019616](https://doi.org/10.1029/2004GL019616).

1071 Ukhorskiy, A. Y., K. Takahashi, B. J. Anderson, and H. Korth (2005), Impact of toroidal ULF
1072 waves on the outer radiation belt electrons, J. Geophys. Res., 110, A10202,
1073 doi:[10.1029/2005JA011017](https://doi.org/10.1029/2005JA011017).

1074 Ukhorskiy, A. Y., B. J. Anderson, P. C. Brandt, and N. A. Tsyganenko (2006), Storm time
1075 evolution of the outer radiation belt: Transport and losses, J. Geophys. Res., 111, A11S03,
1076 doi:[10.1029/2006JA011690](https://doi.org/10.1029/2006JA011690).

1077 Vassiliadis, D., S. F. Fung, and A. J. Klimas (2005), Solar, interplanetary, and magnetospheric
1078 parameters for the radiation belt energetic electron flux, J. Geophys. Res., 110, A04201,
1079 doi:[10.1029/2004JA010443](https://doi.org/10.1029/2004JA010443).

1080 Vennerstrøm, S. (1999), Dayside magnetic ULF power at high latitudes: A possible long-term

1081 proxy for the solar wind velocity?, *J. Geophys. Res.*, 104(A5), 10145–10157,
1082 doi:[10.1029/1999JA900015](https://doi.org/10.1029/1999JA900015).

1083 Wing, S., Johnson, J. R., Jen, J., Meng, C.-I., Sibeck, D. G., Bechtold, K., Freeman, J., Costello,
1084 K., Balikhin, M., and Takahashi, K. (2005), Kp forecast models, *J. Geophys. Res.*, 110,
1085 A04203, doi:[10.1029/2004JA010500](https://doi.org/10.1029/2004JA010500).

1086 Wing, S., J. R. Johnson, C. C. Chaston, M. Echim, C. P. Escoubet, B. Lavraud, C. Lemon, K.
1087 Nykyri, A. Otto, J. Raeder, and C.-P. Wang (2014), Review of solar wind entry into and
1088 transport within the plasma sheet, *Space Science Reviews*, 184, 33 – 86,
1089 doi:10.1007/s11214-014-0108-9

1090 Wing, S., J. R. Johnson, E. Camporeale, and G. D. Reeves (2016), Information theoretical
1091 approach to discovering solar wind drivers of the outer radiation belt, *J. Geophys. Res. Space*
1092 *Physics*, 121, 9378–9399, doi:[10.1002/2016JA022711](https://doi.org/10.1002/2016JA022711)

1093 Wing, S., J. Johnson, and A. Vourlidas (2018), Information theoretic approach to discovering
1094 causalities in the solar cycle, *Ap J*, **854**, 85, <https://doi.org/10.3847/1538-4357/aaa8e7>

1095 Wing, S., J. R. Johnson (2019), Applications of Information Theory in Solar and Space
1096 Physics, *Entropy*, 21(2):140, <https://doi.org/10.3390/e21020140>

1097 Wing, S., P. C. Brandt, D. G. Mitchell, J. R. Johnson, W. S. Kurth and J. D. Menietti (2020),
1098 Periodic Narrowband Radio Wave Emissions and Inward Plasma Transport at Saturn’s
1099 Magnetosphere, *Ap J*, 159, 249, 10.3847/1538-3881/ab818d, [https://doi.org/10.3847/1538-](https://doi.org/10.3847/1538-3881/ab818d)
1100 [3881/ab818d](https://doi.org/10.3847/1538-3881/ab818d)

1101 Wyner, A. D. (1978), A definition of conditional mutual information for arbitrary ensembles, *Info.*
1102 *and Control*, 38, 51–59.

1103 Xiang, Z., Tu, W., Li, X., Ni, B., Morley, S. K., & Baker, D. N. (2017). Understanding the

1104 mechanisms of radiation belt dropouts observed by Van Allen Probes. *Journal of*
1105 *Geophysical Research: Space*
1106 *Physics*, 122, 9858– 9879. <https://doi.org/10.1002/2017JA024487>

1107 Xiang, Z., Tu, W., Ni, B., Henderson, M. G., & Cao, X. (2018). A statistical survey of radiation
1108 belt dropouts observed by Van Allen Probes. *Geophysical Research Letters*, 45.
1109 <https://doi.org/10.1029/2018GL078907>

1110 Zhao, H., Baker, D. N., Jaynes, A. N., Li, X., Elkington, S. R., Kanekal, S. G., Spence, H.
1111 E., Boyd, A. J., Huang, C.-L., and Forsyth, C. (2017), On the relation between radiation belt
1112 electrons and solar wind parameters/geomagnetic indices: Dependence on the first adiabatic
1113 invariant and L^* , *J. Geophys. Res. Space Physics*, 122, 1624– 1642,
1114 doi:[10.1002/2016JA023658](https://doi.org/10.1002/2016JA023658).

1115 Zhao, H., Baker, D. N., Li, X., Jaynes, A. N., & Kanekal, S. G. (2018). The acceleration of
1116 ultrarelativistic electrons during a small to moderate storm of 21 April 2017. *Geophysical*
1117 *Research Letters*, 45, 5818– 5825. <https://doi.org/10.1029/2018GL078582>

1118

1119

rank	solar wind and magnetospheric parameters	i_{tr_max}	peak τ (hour)
1	V_{sw}	0.12	46
2	SYM-H	0.030	20–60
3	AL	0.020	50–80
4	P_{dyn}^a	0.018	7–11
5	IMF $ B ^a$	0.018	50–110
6	IMF $B_z < 0^a$	0.017	50–110
7	n_{sw}^a	0.016	7–11
8	IMF B_y^a	0.012	0–16
9	Esw	0.012	40–90
10	IMF $B_z > 0$	0.011	0–16
11	$\sigma(\text{IMF B})$	0.0083	0–10

1121
1122
1123
1124
1125
1126
1127
1128
1129
1130
1131
1132

Table 1. Ranking of the the solar wind and magnetospheric parameters based on information transfer to radiation belt electron PSD. Parameters 2–11 are calculated from $\text{CMI}(x \rightarrow \text{PSD} | V_{sw})$ where $x = \text{IMF } |B|, B_z < 0, B_z > 0, B_y, \text{Esw}, \text{ and } \sigma(\text{IMF B})$. Parameter 1 from $\text{CMI}(V_{sw} \rightarrow \text{PSD} | n_{sw})$. $i_{tr_max} = \text{peak CMI} - \text{mean noise}$ where noise is calculated for surrogate data (see Section 4.1).

^a the response has dual mode: at small τ ($\tau < 15$ hr) the response is electron loss and at large τ ($\tau > 40$ hr) the response is electron enhancement. The ranking is based on the larger i_{tr_max} of the two responses (see text for explanation).

Parameters	Correlation	Peak τ (hr)	Conditional Mutual Information (CMI)	Peak τ (hr)
V_{sw}	corr($V_{sw} \rightarrow \text{PSD}$)	38	CMI($V_{sw} \rightarrow \text{PSD} n_{sw}$)	46
n_{sw}	corr($n_{sw} \rightarrow \text{PSD}$)	15	CMI($n_{sw} \rightarrow \text{PSD} V_{sw}$)	7
AL	corr(AL \rightarrow PSD)	53	CMI(AL \rightarrow PSD V_{sw})	76
SYM-H	corr(SYM-H \rightarrow PSD)	40	CMI(SYM-H \rightarrow PSD V_{sw})	55

1133

1134

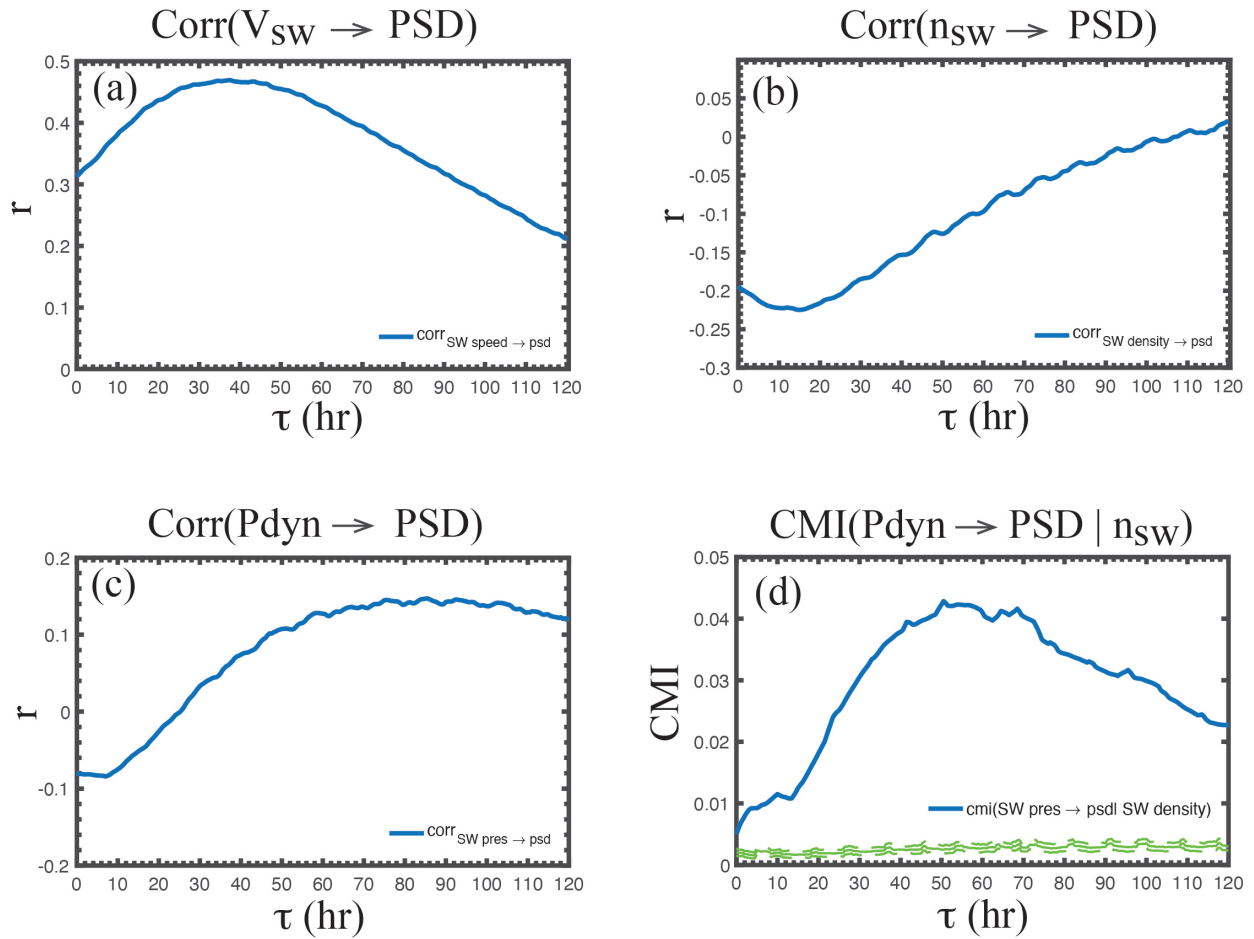
1135

1136

1137

Table 2. Highlighting the differences between correlation and CMI. τ is the radiation belt response lag time.

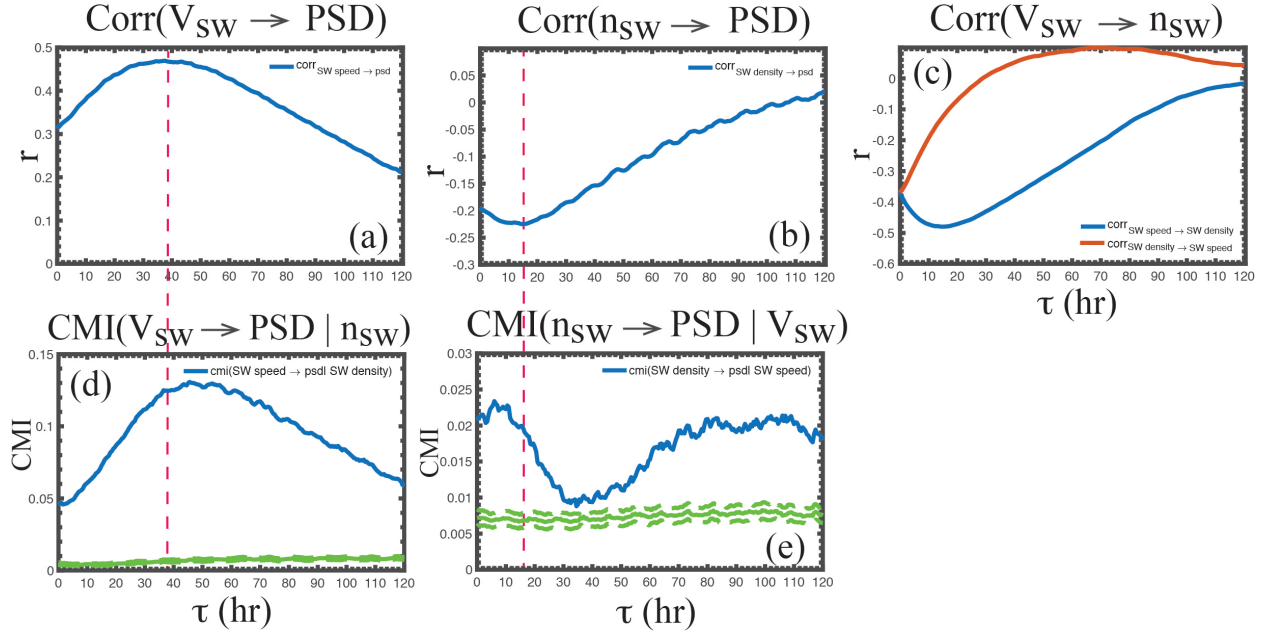
1138
1139



1140

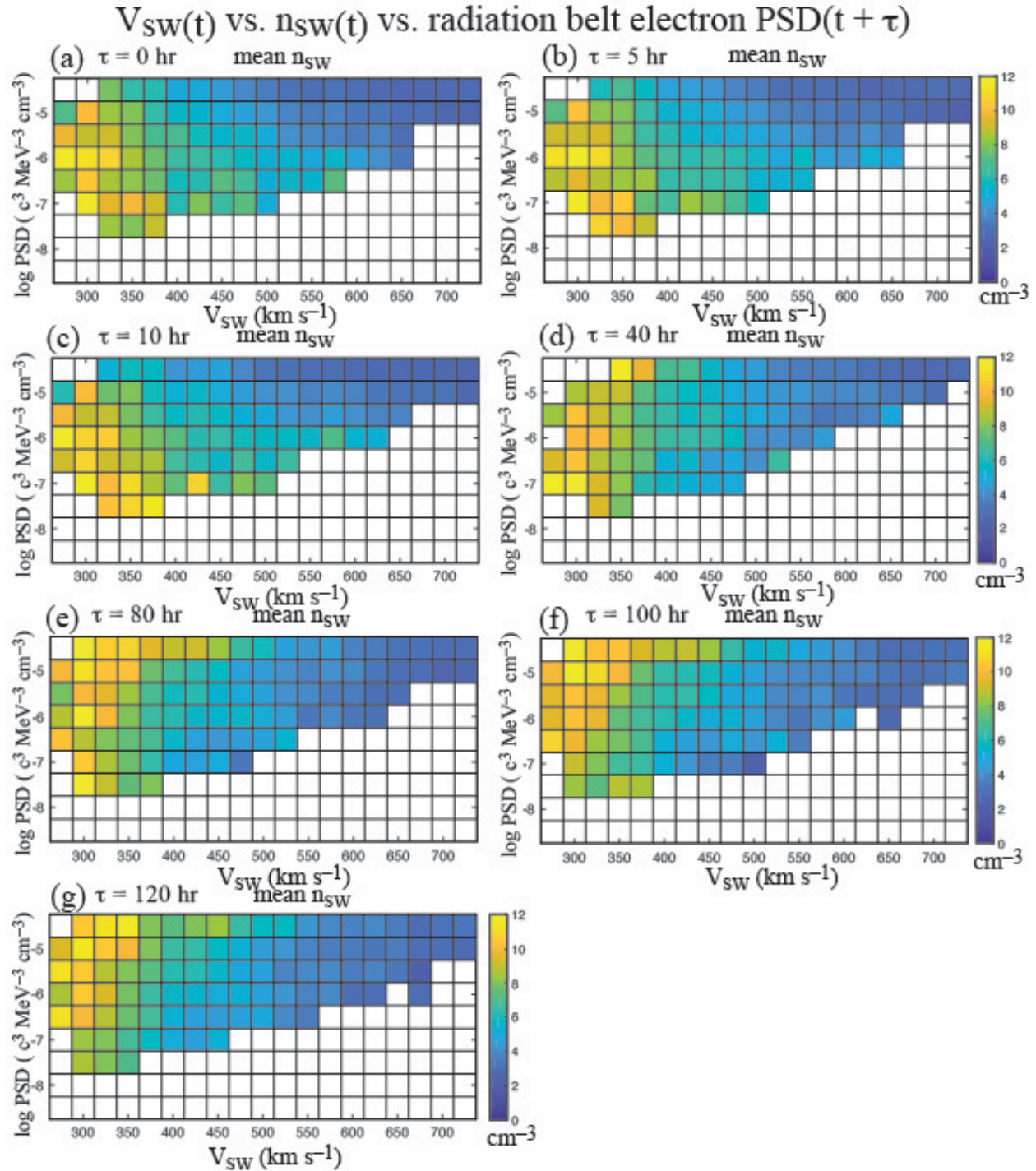
1141 Figure 1. (a) V_{sw} positively correlates with radiation belt electron PSD. (b) n_{sw} negatively
1142 correlates with PSD. (c) The PSD response to solar wind dynamic pressure (P_{dyn}) has two modes:
1143 at small τ , P_{dyn} negatively correlates with PSD, similar to n_{sw} while at large τ , P_{dyn} positively
1144 correlates with PSD, similar to V_{sw} . (d) $\text{CMI}(P_{dyn} \rightarrow \text{PSD} | V_{sw})$ is plotted as the blue curve. It
1145 shows that removing the effect of V_{sw} , the information transfer from P_{dyn} to PSD is similar to V_{sw}
1146 correlation with PSD, as expected. The mean noise and 3σ from the noise are plotted as solid and
1147 dashed green curves, respectively. The peak of the blue curve is 203σ above the mean noise and
1148 hence significant.
1149

The effects of V_{SW} and n_{SW} on radiation belt electron psd



1150
1151

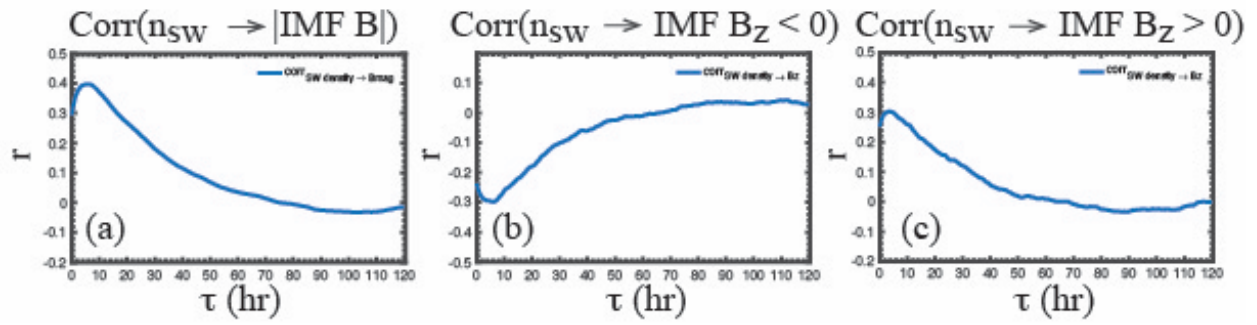
1152 Figure 2. (a) V_{SW} positively correlates with PSD (same as Figure 1a). (b) n_{SW} negatively correlates
1153 with PSD (same as Figure 1b). (c) $\text{corr}(V_{SW} \rightarrow n_{SW}) =$ blue curve and $\text{corr}(n_{SW} \rightarrow V_{SW}) =$ red curve.
1154 The negative correlation between V_{SW} and n_{SW} raises the question that (a) or (b) may be coincidental.
1155 (d) $\text{CMI}(V_{SW} \rightarrow \text{PSD} | n_{SW})$ shows that (1) there is still information transfer from V_{SW} to PSD even
1156 after the effect of n_{SW} is removed and (2) removing the effect of n_{SW} shifts the peak of $\text{corr}(V_{SW} \rightarrow$
1157 $\text{PSD})$ to the right. (e) $\text{CMI}(n_{SW} \rightarrow \text{PSD} | V_{SW})$ shows that (1) there is still information transfer from
1158 n_{SW} to PSD even after the effect of V_{SW} is removed and (2) removing the effect of V_{SW} shifts the peak
1159 of $\text{corr}(n_{SW} \rightarrow \text{PSD})$ to the left. The red dashed vertical lines help visualize the shifts of the peaks
1160 in the correlations. $\text{CMI}(n_{SW} \rightarrow \text{PSD} | V_{SW})$ has a secondary peak at $\tau = 80-120$ hr. The mean noise
1161 and 3σ from the noise are plotted as solid and dashed green curves, respectively.



1162

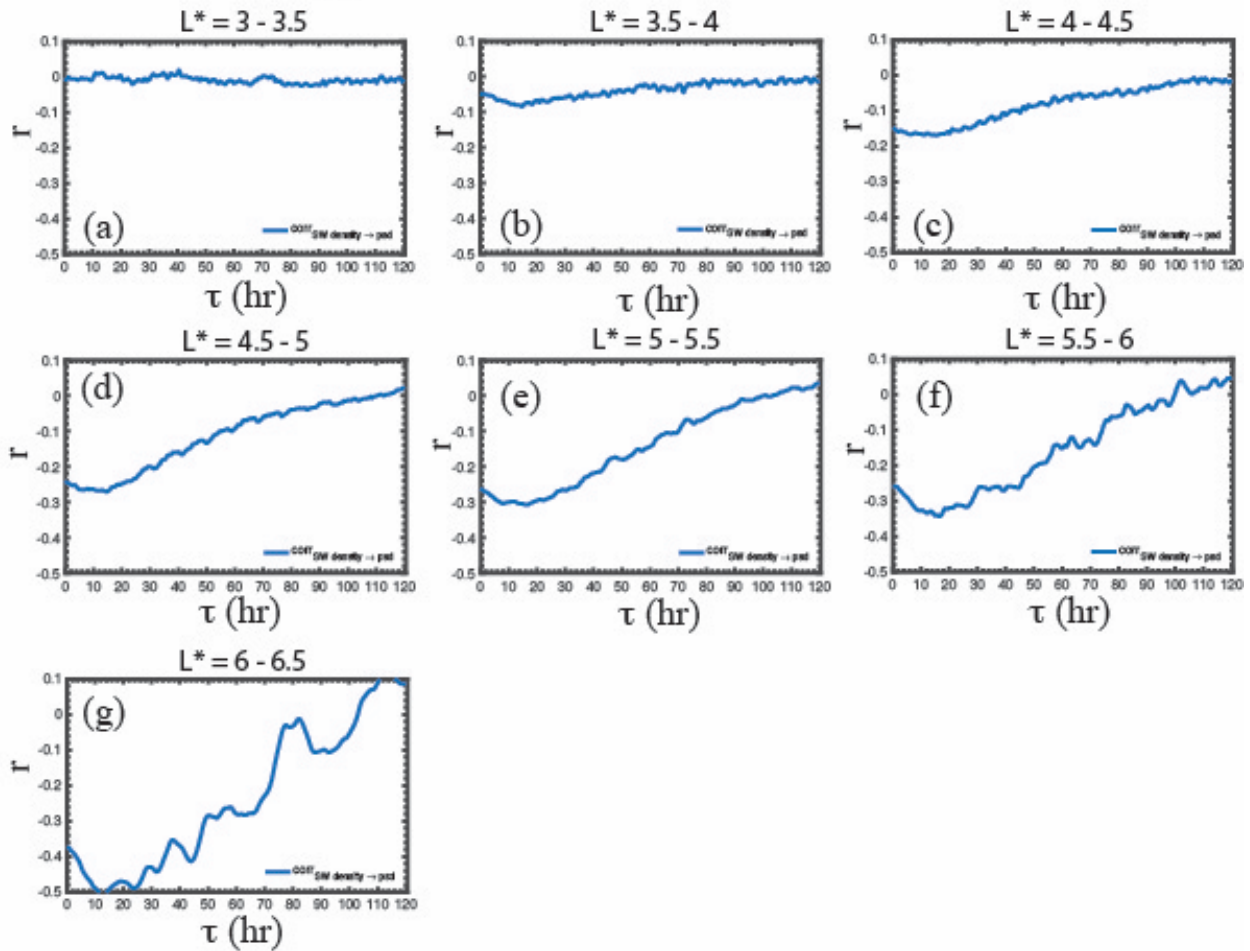
1163 Figure 3. (a–g) log PSD($t + \tau$) vs. $V_{SW}(t)$ vs. $n_{SW}(t)$ for $\tau = 0, 5, 10, 40, 80, 100,$ and 120 hr,
 1164 respectively. The color is n_{SW} . Large V_{SW} ($V_{SW} > 450 \text{ km s}^{-1}$) corresponds to high PSD. For small
 1165 V_{SW} ($V_{SW} < 450 \text{ km s}^{-1}$), at small τ ($\tau = 0, 5, 10$ hr), n_{SW} negatively correlates with PSD, but at large
 1166 τ ($\tau = 80, 100, 120$ hr), n_{SW} positively correlates with PSD. At $\tau = 40$, the correlation is weak.
 1167 Figure 3 is consistent with $\text{CMI}(n_{SW} \rightarrow \text{PSD} | V_{SW})$ plotted in Figure 2e.

The effects of n_{SW} and IMF B_z on radiation belt electron PSD



1168

1169 Figure 4. (a) n_{SW} positively correlates with $|\text{IMF } B|$. (b) n_{SW} negatively correlates with $\text{IMF } B_z < 0$.
 1170 (c) n_{SW} positively correlates with $\text{IMF } B_z > 0$.
 1171

Correlation of n_{SW} and radiation belt electron PSD as a function of L^* 

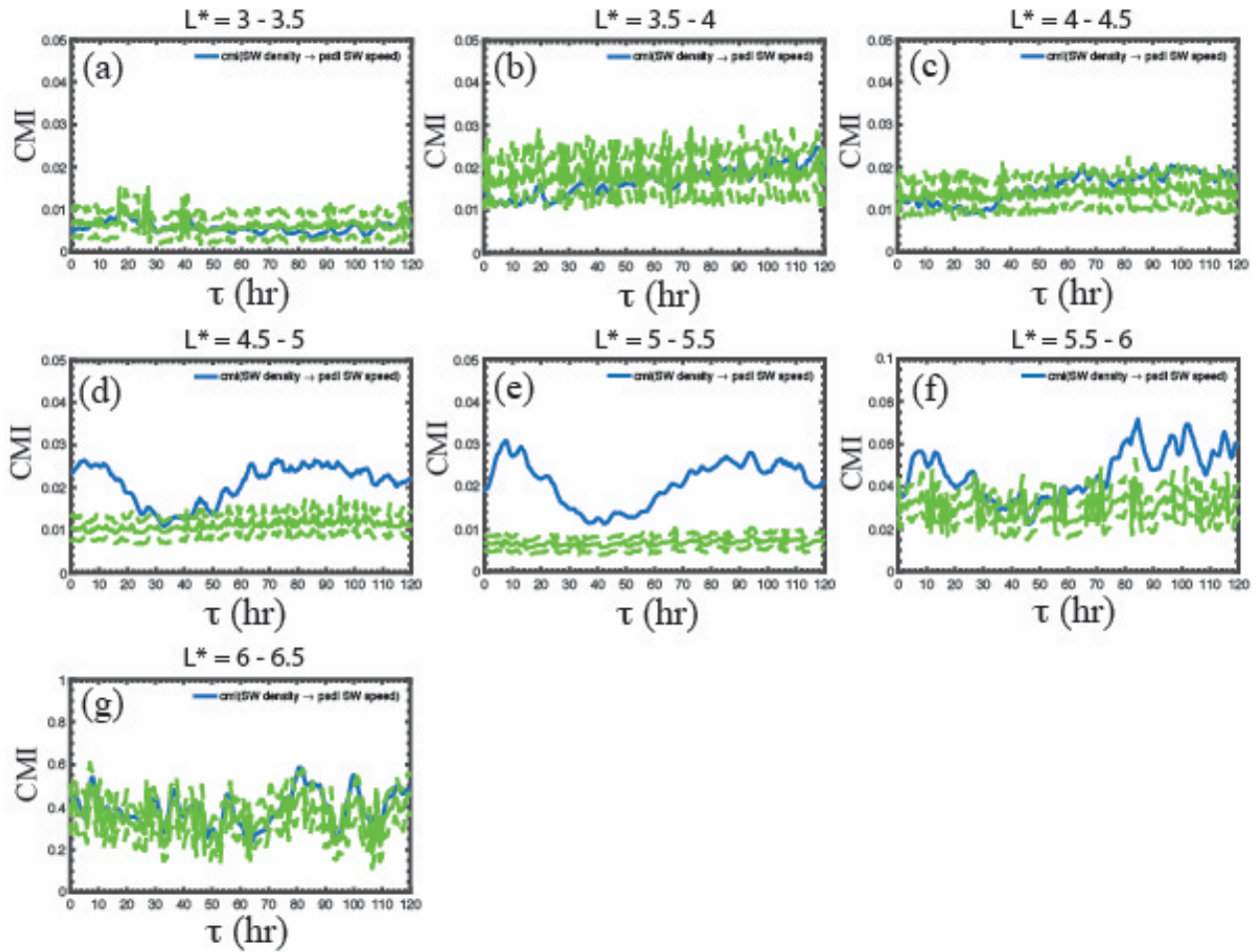
1173

1174

1175 Figure 5. $\text{corr}(n_{SW} \rightarrow \text{PSD})$ from $L^* = 3$ to 6.5 in seven bins each with width = 0.5. (a) The
 1176 correlation is insignificant at $L^* = 3-3.5$, but slowly increases with increasing L^* . (b-g) The
 1177 correlations are significant ($p < 0.01$) at the minimum τ ($\tau = 15, 16, 17, 17, 17, 13$ hr), $r = (-0.086,$
 1178 $-0.17, -0.27, -0.31, -0.34, -0.50)$, and $n = (8,302, 11,481, 17,7891, 27,060, 6,236, 528),$
 1179 respectively.

1180

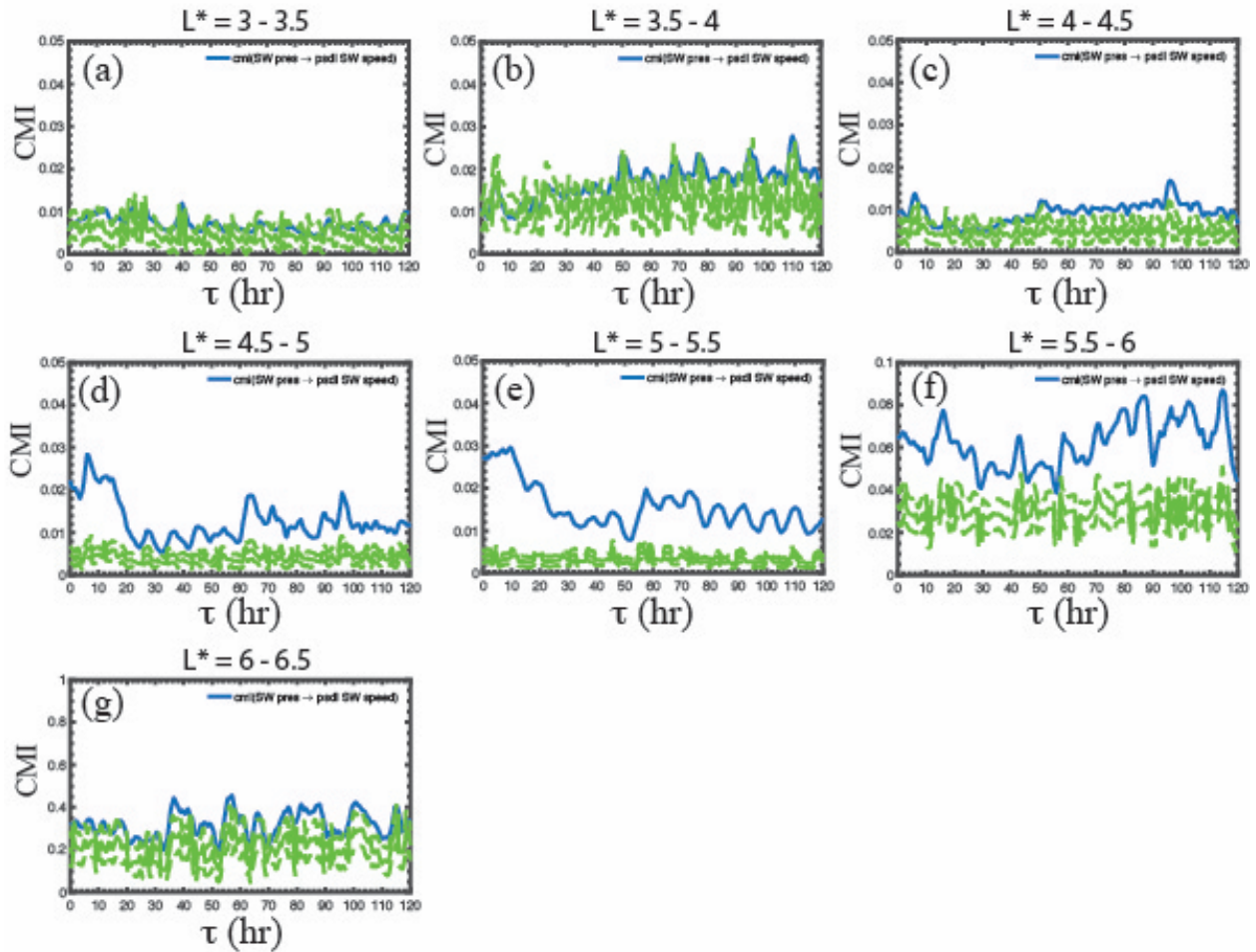
CMI($n_{sw} \rightarrow \text{PSD} | V_{sw}$) as a function of L^*



1181
 1182 Figure 6. CMI($n_{sw} \rightarrow \text{PSD} | V_{sw}$) from $L^* = 3$ to 6.5 in seven bins each having width = 0.5. The
 1183 mean noise and 3σ from the noise are plotted as solid and dashed green curves, respectively. (a)
 1184 The CMI is at the noise level at $L^* = 3-3.5$, which is consistent with the correlation in Figure 5a.
 1185 (b-c) CMI is at the noise level at $L^* = 3.5-4.5$, unlike the correlation in Figures 5a and 5b. (d-e)
 1186 The peak CMI is significant at $L^* = 4.5-5.5$ and (f) barely significant at $L^* = 5.5-6$. (g) The CMI
 1187 is at the noise level at $L^* = 6-6.5$ where there is a large variability in PSD at this outermost L^*
 1188 layer.

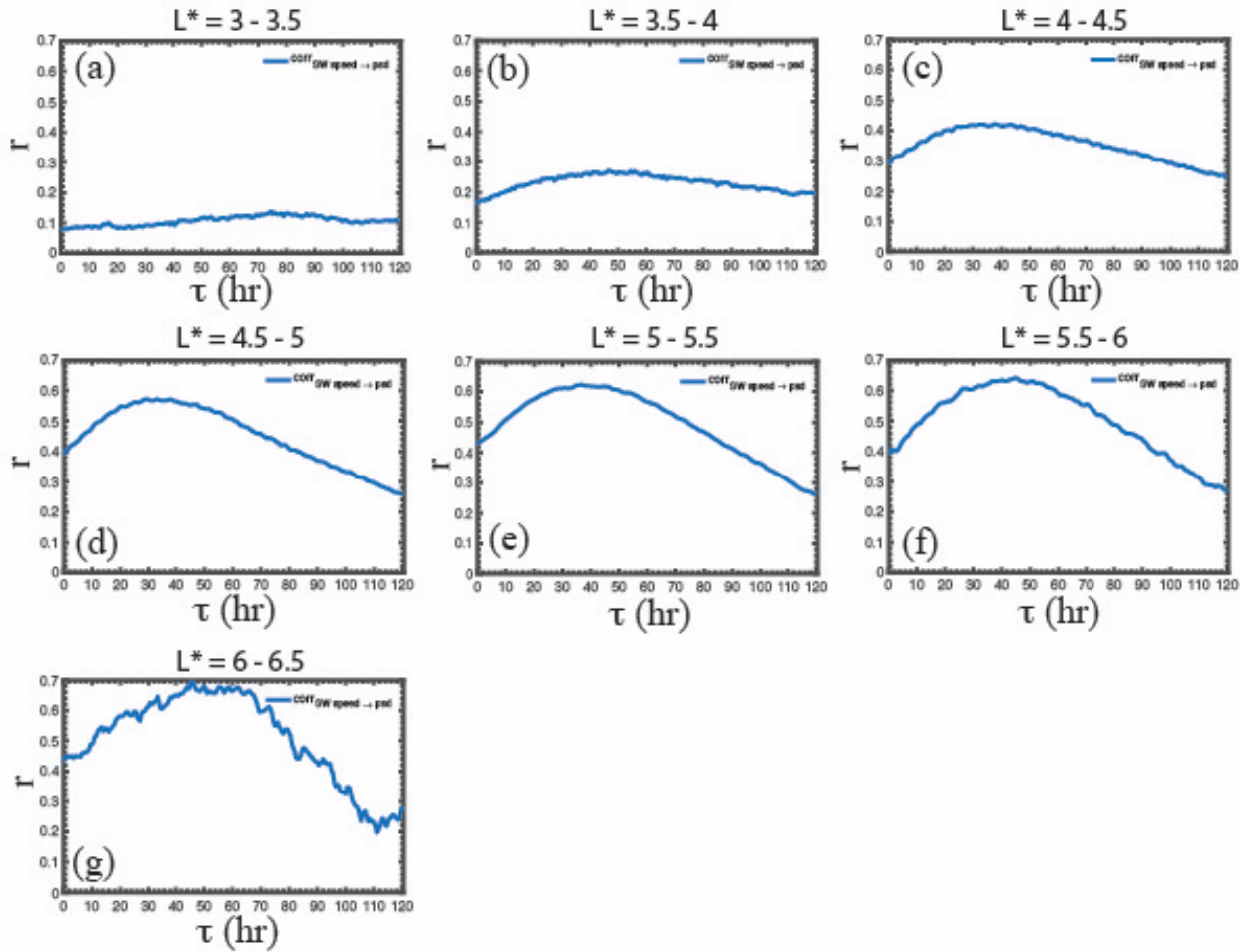
1189
 1190
 1191
 1192
 1193

CMI($P_{dyn} \rightarrow PSD | V_{sw}$) as a function of L^*



1194
 1195 Figure 7. CMI($P_{dyn} \rightarrow PSD | V_{sw}$) from $L^* = 3$ to 6.5 in seven bins in the same format as in Figure
 1196 6. The mean noise and 3σ from the noise are plotted as solid and dashed green curves, respectively.
 1197 Similar to their counterparts in Figure 6 panels d–f, the primary peak CMIs are significant only at
 1198 $L^* = 4.5$ –5.5 (d–e) and barely significant at $L^* = 5.5$ –6. The significances at $L^* = 4.5$ –6 are higher
 1199 than their counterparts in Figures 6 panels d–f for CMI($n_{sw} \rightarrow PSD | V_{sw}$), suggesting that P_{dyn} is
 1200 the real causal variable rather than n_{sw} . The opposite is true for the secondary peak, suggesting the
 1201 causal variable is related more to n_{sw} rather than P_{dyn} .

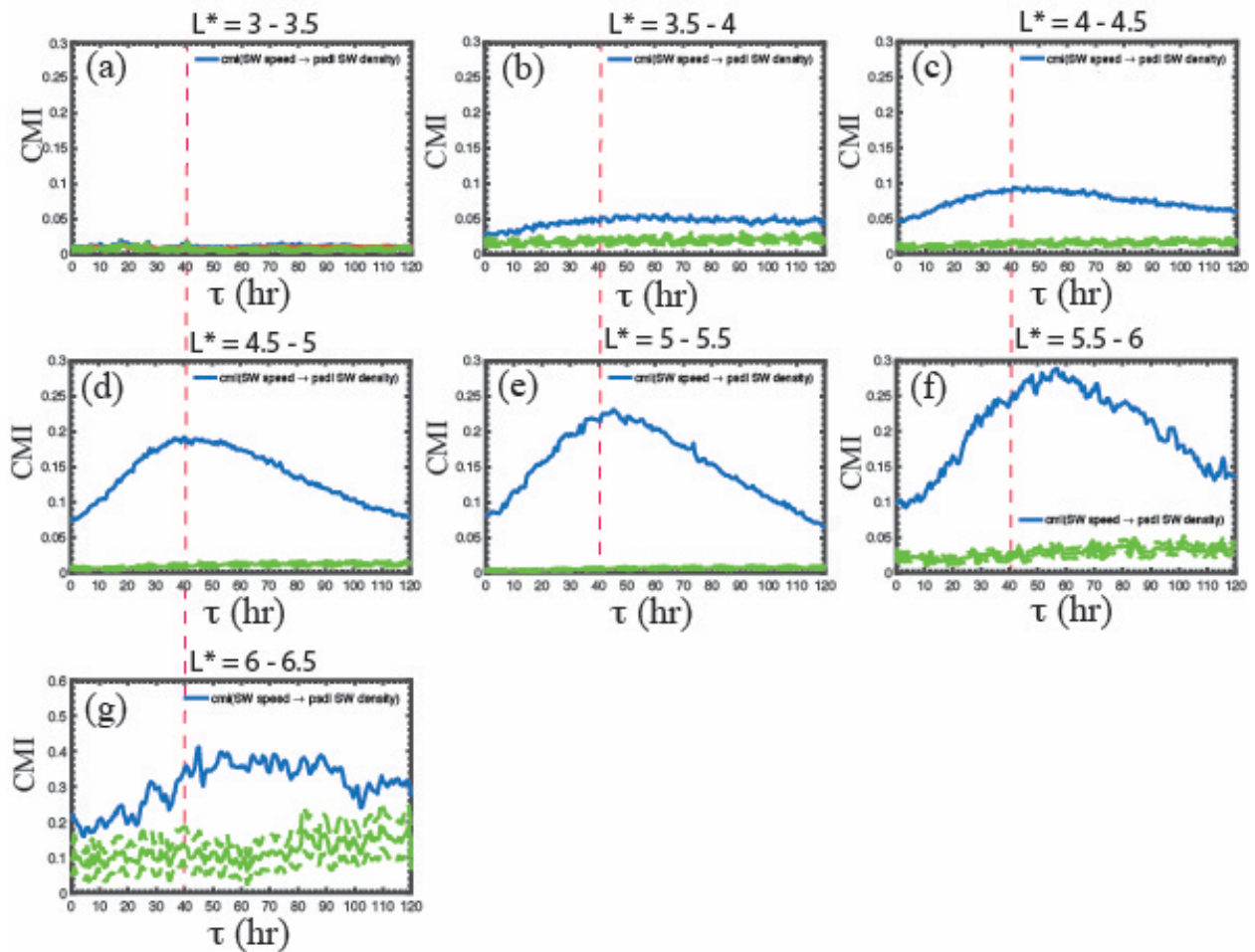
Correlation of V_{SW} and radiation belt electron PSD as a function of L^*



1202
1203

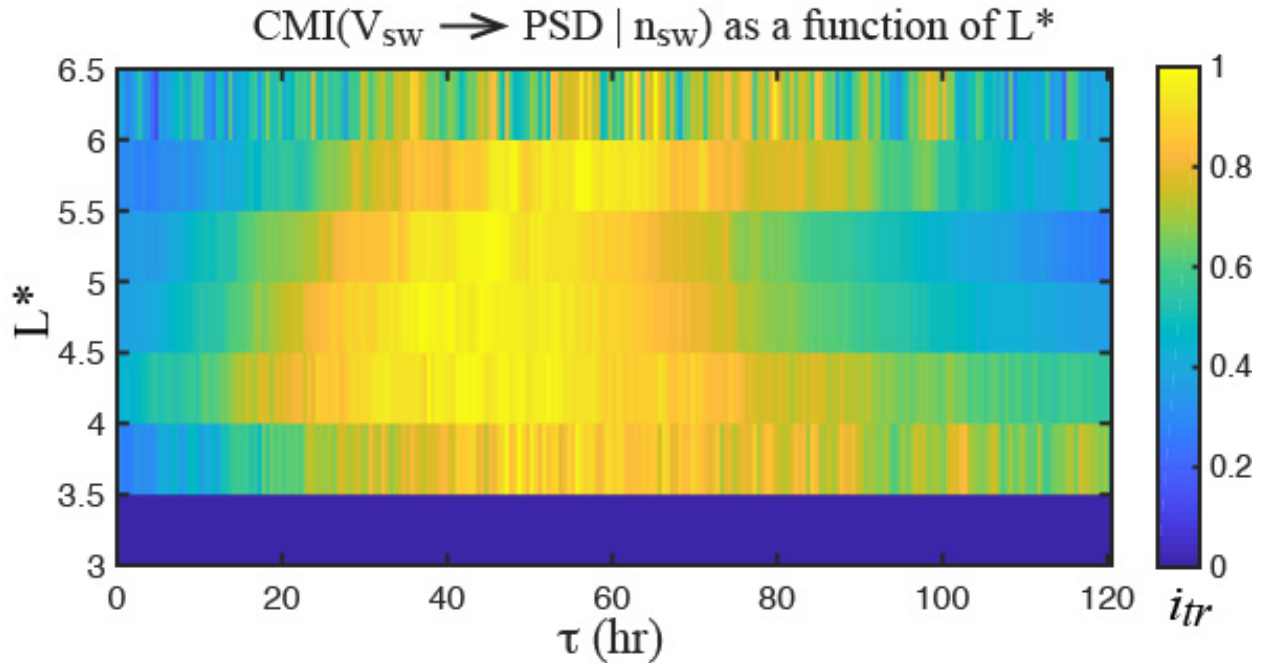
1204 Figure 8. $\text{corr}(V_{SW} \rightarrow \text{PSD})$ from $L^* = 3$ to 6.5 in seven bins in the same format as Figure 5. (a–
1205 g) The correlations are all significant at $p < 0.01$ at the maximum τ ($\tau = 40$ – 120 , 30 – 120 , 38 , 30 ,
1206 37 , 45 , 30 – 90 hr), ($r = 0.14, 0.27, 0.42, 0.57, 0.62, 0.64, 0.70$) for $L^* = 3$ – $3.5, 3.5$ – $4, 4$ – $4.5, 4.5$ –
1207 $5, 5$ – $5.5, 5.5$ – $6, \text{ and } 6$ – 6.5 , respectively.
1208

CMI($V_{sw} \rightarrow \text{PSD} | n_{sw}$) as a function of L^*



1209
 1210
 1211
 1212
 1213
 1214
 1215
 1216
 1217
 1218
 1219
 1220
 1221
 1222
 1223

Figure 9. CMI($V_{sw} \rightarrow \text{PSD} | n_{sw}$) from $L^* = 3$ to 6.5 in seven bins in the same format as Figure 6. The mean noise and 3σ from the noise are plotted as solid and dashed green curves, respectively. (a) The CMI is at the noise level at $L^* = 3-3.5$, unlike the correlation in Figure 8a. (b-c) At $L^* = 3.5-4.5$, the CMI has broad peaks from $\tau \sim 50$ to 100 hr (or larger in the case $L^* = 3.5 - 4$) and the peaks are significant. (d-f) At $L^* = 4.5-6$, the CMI peaks are narrower (peak $\tau = 40, 46, 57$ hr, respectively). (g) At $\tau = 6-6.5$, the peak broadens again but remains significant.

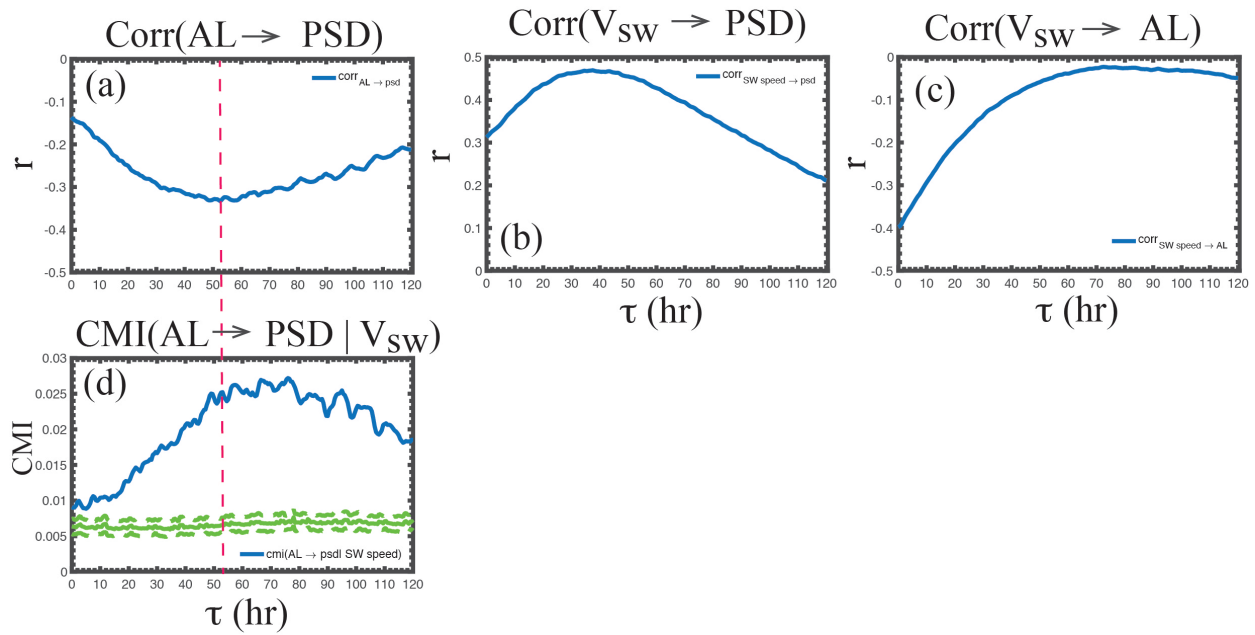


1224
 1225
 1226
 1227
 1228
 1229
 1230
 1231
 1232
 1233
 1234

Figure 10. The normalized i_{tr} as a function of L^* and τ where i_{tr} = the amount of information transferred = $\text{CMI}(V_{sw} \rightarrow \text{PSD} | n_{sw}) - \text{mean noise}$ (the blue curve subtracted by the solid green curve in Figure 9). The orange and yellow correspond roughly to the top 20% of i_{tr} in each L^* bin. The smallest peak τ can be found at $L^* = 4.5 - 5.5$ where $\tau = 35 - 50$ hr. The peak τ broadens and shifts to larger τ at higher L^* ($t = 45 - 65$ and $40 - 100$ hr for $L^* = 5.5 - 6$ and $6 - 6.5$, respectively) and lower L^* ($\tau = 35 - 55$ and $45 - 60$ hr for $L^* = 4 - 4.5$ and $3.5 - 4$, respectively). The broadening and shifting of the peak to higher τ may suggest outward and inward diffusion from $L^* = 4.5 - 5.5$. At $L^* = 4 - 4.5$, peak τ starts about the same time as that at $L^* = 4.5 - 5.5$, which is suggestive of local acceleration at this L^* band as well.

1235

The effect of AL on radiation belt electron PSD



1236

1237

1238 Figure 11. (a) AL negatively correlates with radiation belt electron PSD. (b) V_{sw} positively

1239 correlates with PSD (same as Figure 1a). (c) V_{sw} negatively correlates with AL. Given (b) and (c),

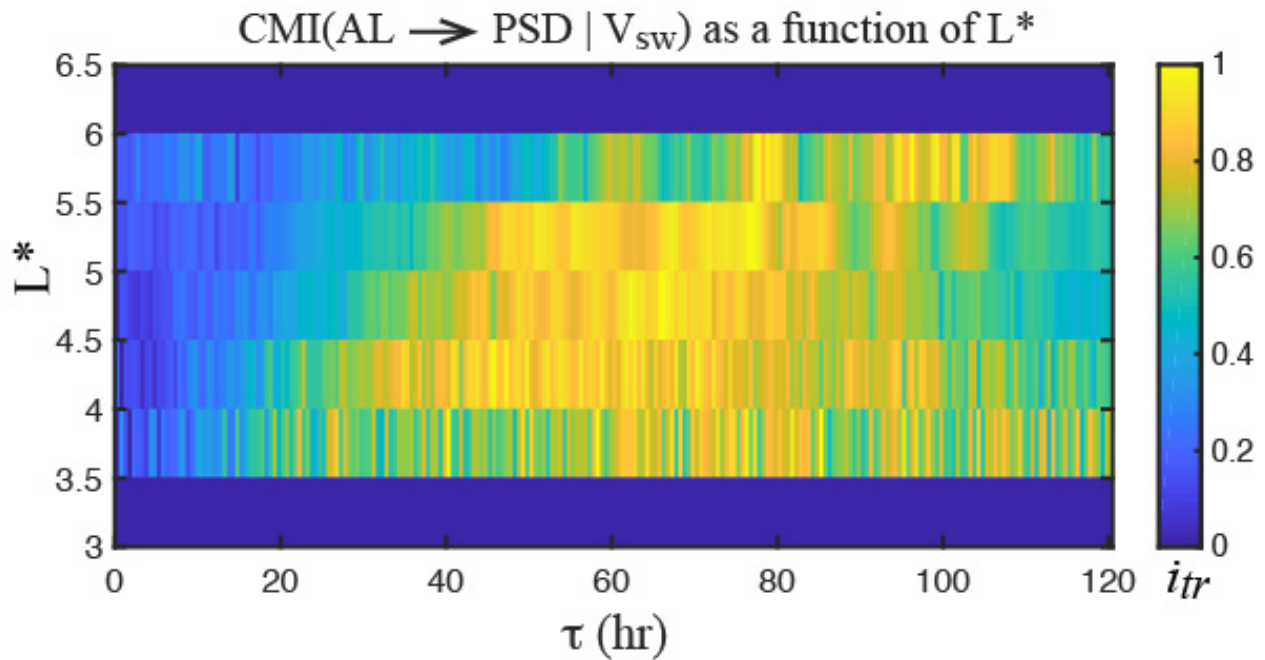
1240 the correlation in (a) may just be coincidental. (d) CMI(AL \rightarrow PSD | V_{sw}) shows that even after

1241 the effect of V_{sw} has been removed, AL still has an effect on PSD. The mean noise and 3σ from

1242 the noise are plotted as solid and dashed green curves, respectively.

1243

1244



1245

1246

1247

1248

1249

1250

1251

1252

1253

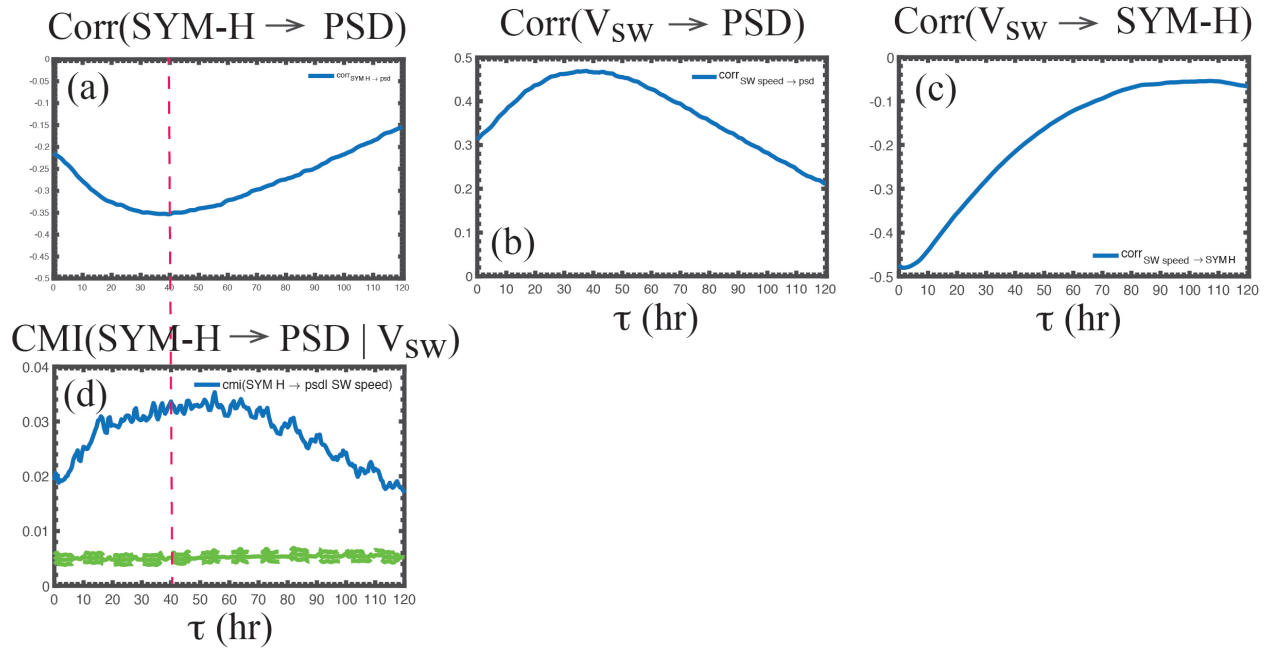
1254

1255

Figure 12. The normalized i_{tr} as a function of L^* and τ where i_{tr} = the amount of information transferred = $\text{CMI}(\text{AL} \rightarrow \text{PSD} | V_{sw}) - \text{mean noise}$ in the same format as Figure 10. The orange and yellow correspond roughly to the top 20% of i_{tr} in each L^* bin. The i_{tr} is at the noise level at $L^* = 3-4$ and $6-6.5$. The region with the largest significance is $L^* = 4.5-5$ and $5-5.5$ with $\tau = 40-80$ and $45-85$ hr, respectively. The peak shifts to higher τ , $\tau = 75-100$ hr, at $L^* = 5.5-6$, suggesting outward diffusion from $L^* = 4.5-5.5$. At $L^* = 4-4.5$, the peak is the broad at $\tau = 35-80$ hr. Because the peak τ starts about the same time as that at $L^* = 4.5-5$, it may suggest local acceleration at this L^* . The slow decay of τ suggests inward diffusion or longer lasting wave activity.

1256

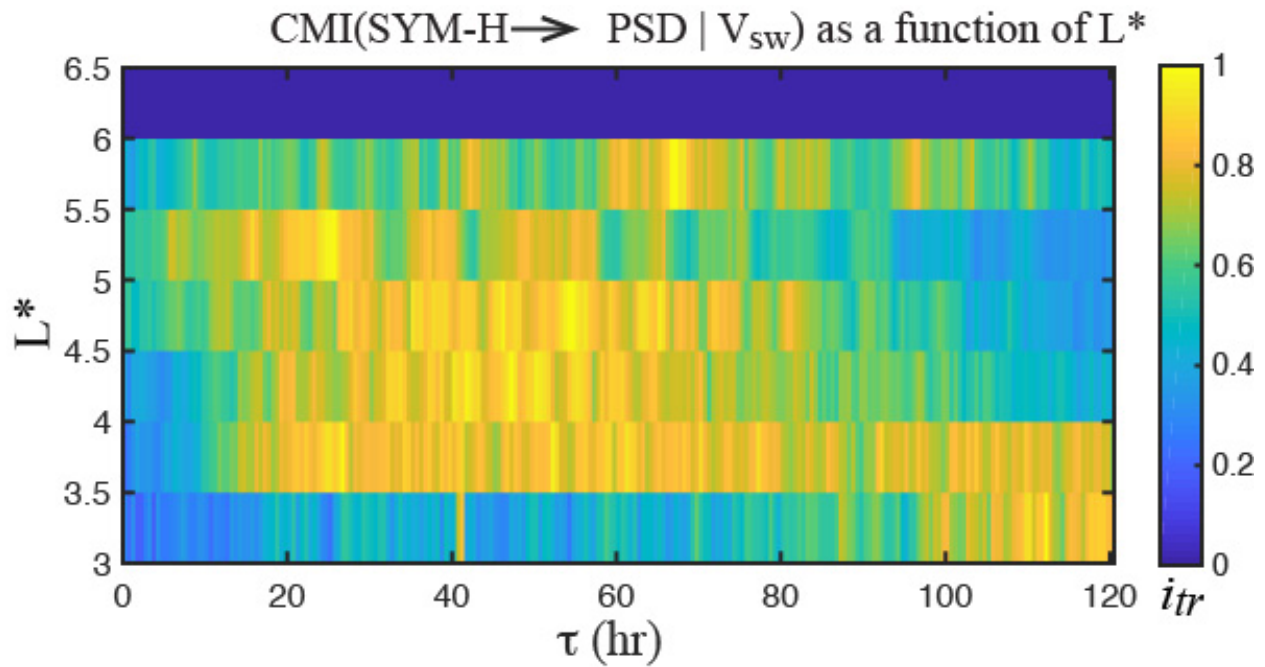
The effect of Sym-H on radiation belt electron PSD



1257
1258
1259
1260
1261
1262
1263

Figure 13. (a) SYM-H negatively correlates with radiation belt electron PSD. (b) V_{sw} positively correlates with PSD (same as Figure 1a). (c) V_{sw} negatively correlates with SYM-H. Given (b) and (c), the correlation in (a) may just be coincidental. (d) $\text{CMI}(\text{SYM-H} \rightarrow \text{PSD} | V_{sw})$ shows that even after the effect of V_{sw} has been removed, SYM-H still has an effect on PSD. The mean noise and 3σ from the noise are plotted as solid and dashed green curves, respectively.

1264



1265

1266

1267

1268

1269

1270

1271

1272

1273

1274

1275

1276

1277

Figure 14. The normalized i_{tr} as a function of L^* and τ where i_{tr} = the amount of information transferred = $\text{CMI}(\text{SYM-H} \rightarrow \text{PSD} | V_{sw}) - \text{mean noise}$ in the same format as Figure 10. The orange and yellow correspond roughly to the top 20% of i_{tr} in each L^* bin. The i_{tr} is at the noise level at $L^* = 6-6.5$ where there is a large variability in the radiation belt electron PSD. The highest peak significance can be found at $L^* = 5-5.5$ with $\tau = 20-55$ hr. The peak broadens and shifts to higher τ , $\tau = 60-75$ hr at $L^* = 5.5-6$, suggesting outward diffusion from $L^* = 5-5.5$. At $L^* = 4-4.5$ and $4.5-5$, the i_{tr} peaks at $\tau = 30-60$ and $30-75$ hr. At $L^* = 3.5-4$, the peak is very broad at $\tau = 20-120$ hr, which may suggest local acceleration and inward diffusion from higher L^* . At $L^* = 3-3.5$, the i_{tr} peaks at $\tau = 110-120$ hr or may be even higher, which may suggest slow diffusion from higher L^* .